December 2016

Sensitivity Analysis of Geometry Changes in the Simulation of Basilar Aneurysms

Paul Eserkaln
University of Wisconsin-Milwaukee

SENSITIVITY ANALYSIS OF GEOMETRY CHANGES IN THE SIMULATION OF BASILAR ANEURYSMS

by

Paul Eserkaln

A Thesis Submitted in

Partial Fulfillment of the

Requirements for the Degree of

Master of Science

in Engineering

at

University of Wisconsin-Milwaukee

December 2016

ABSTRACT

SENSITIVITY ANALYSIS OF GEOMETRY CHANGES IN THE SIMULATION OF BASILAR ANEURYSMS

by

Paul Eserkaln

The University of Wisconsin-Milwaukee, 2016
Under the Supervision of Professor Vitaliy Rayz and Professor Anoop Dhingra

Computer simulation is a useful tool in the research and treatment of basilar aneurysms. Current technology allows researchers to create 3D models from cerebral vasculature in-vivo, allowing for the investigation of surgical options with minimal risk to the patient. The method used to construct these models overlooks smaller lateral arterial branches which are difficult to discern due to resolution limits of the imaging process. These lateral branches have minimal impact on the overall blood flow through the basilar artery, but they play a significant role in the health of the patient, so it is important to ensure sufficient blood will reach them after treatment is performed.

In order to simulate the flow through the basilar artery and its branches, these smaller vessels must be added to the model manually. These lateral branches vary widely in size, location, and quantity between patients, but the resulting blood flow patterns through the basilar artery are relatively consistent.

The purpose of this thesis is to gain a better understanding of how differences in the modeling of these lateral branches will affect the overall blood flow patterns both through the basilar artery and the branches themselves. The results of this investigation will help

researchers to make more accurate models when simulating the flow through these lateral branches.

The study was performed through a series of simulations in which the geometric variables in these branches: length, size, quantity, and location were altered and compared. A second set of simulations was performed to further investigate the use of a constant resistance as a replacement for artery length.

The results of the study show that the flow resistance due to the length of an artery could be approximated using a constant pressure, but some wall length must be present in the model to avoid causing a flow disturbance. The location of the vessels did not appear to have a significant impact on the flow patterns. Increasing the number of arteries results in an overall increase in outlet area, which causes a reduction in blood velocity exiting the basilar artery. No other significant changes in the flow patterns were observed. Altering the size of the vessels had a similarly predictable change in flow distribution, with a greater increase in flow per area increase, which follows Poiseuille's model for laminar flow through tubes.

The results from the second series of simulations verified that modifying the static distal pressure at an artery could accurately replace adjusting the artery length. These studies showed the importance of accounting for the flow distribution, the recirculation regions, and the flow mixing when determining this distal outlet pressure.

TABLE OF CONTENTS

LIST OF FIGURES

LIST OF TABLES

ACKNOWLEDGEMENTS

I would like to thank both of my advisors: Professor Vitaliy Rayz and Professor Anoop Dhingra, for their guidance and especially for their patience as I worked through this project. I know it was a struggle, and I am grateful that they never gave up on me.

I am particularly grateful to Professor Rayz for giving me the opportunity to work on this project with him. I learned more from him about running flow simulations, using the Navier-Stokes equations and how the human circulatory system works than I ever thought I would.

I am also grateful for my third committee member Dr. Guilherme Garcia for taking the time to review my work and offer his advice.

My sincerest gratitude goes to Dr. Michael T. Lawton for supplying the raw data used in the simulations. This project would not have been possible without it.

Thank you to Oren and Tyler at CATI for their suggestions and advice on how to best tweak the models and simulation parameters to get better results, as well as a few suggestions for supplemental reading material, some of which ended up in the bibliography.

I am grateful to both Racine Federated and Badger Meter for their support of this endeavor. I would not have pursued this endeavor without their support.

And finally, I wouldn't have been able to make it through this without my very supportive friends and family, particularly my good friend and proofreader Alex Kiedrowicz, and my fiancée Catherine for being very patient and understanding with me this past year. I am fortunate to have such a solid support team.

1. Introduction

Throughout the past several decades, there have been vast improvements in imaging, modeling and simulation technology. These advances have proven to be valuable tools, allowing medical practitioners to diagnose the condition of a patient and assess various options without the need for invasive examination or an experimental treatment plan.

When performing a computer simulation of physiology, the more accurate the representation of the system, the more useful the simulation results will be. As technology advances, simulations can be performed with greater detail, including smaller and smaller features. There are always limits; a minimum size that can be accurately imaged, and a maximum complexity that can be reasonably simulated.

In situations where the size of the features of interest fall below the resolution of the scan but are not beyond the capabilities of the simulation method, approximate versions of these items can be added to the model.

The size and shape of these features can be estimated using data from previous studies, often taken from cadavers. This data will be in the form of statistical averages, not exactly matching the physiology of the patient, but hopefully being close enough for accurate results.

This thesis seeks to identify the effect of changing such things as the size, shape, and location of some of these user-created features in a biological simulation; specifically a simulation of the flow near and around an aneurysm in the basilar artery.

1.1. **Problem Statement**

The purpose of this thesis is to determine how various geometric parameters in the models of the lateral branches of the basilar artery will affect flow behavior in simulations of fusiform basilar aneurysms, both within the basilar artery as well as within the lateral branches themselves. The goals are to identify the key factors governing the flow patterns, determine the relative sensitivity of the flow to changes in the different parameters, and identify major pitfalls or requirements involved in adding these features to the models.

1.2. **Anatomy**

Blood flows into the brain through four primary arteries which merge into a network known as the Circle of Willis (Figure 1-1) which distributes blood to the majority of the brain. The area of interest in this thesis is the basilar artery, which is just below the posterior region of the Circle of Willis. The basilar artery is the junction of the two vertebral arteries (VAs) before they merge into the Circle of Willis. The arteries exiting out from the apex (superior part) of the basilar artery are the two Posterior Cerebral Arteries (PCAs) and the two Superior Cerebral Arteries (SCAs). The majority of the blood flowing into the basilar artery exits through these four outlets to join the Circle of Willis or continue to other portions of the upper brain.

As blood flows through the basilar artery, some portion of it is supplied to the brain stem through smaller arteries which branch from of the basilar artery laterally. These are broadly categorized as the larger Anterior Inferior Cerebral Arteries (AICAs) and smaller Pontine Perforators (perforators).

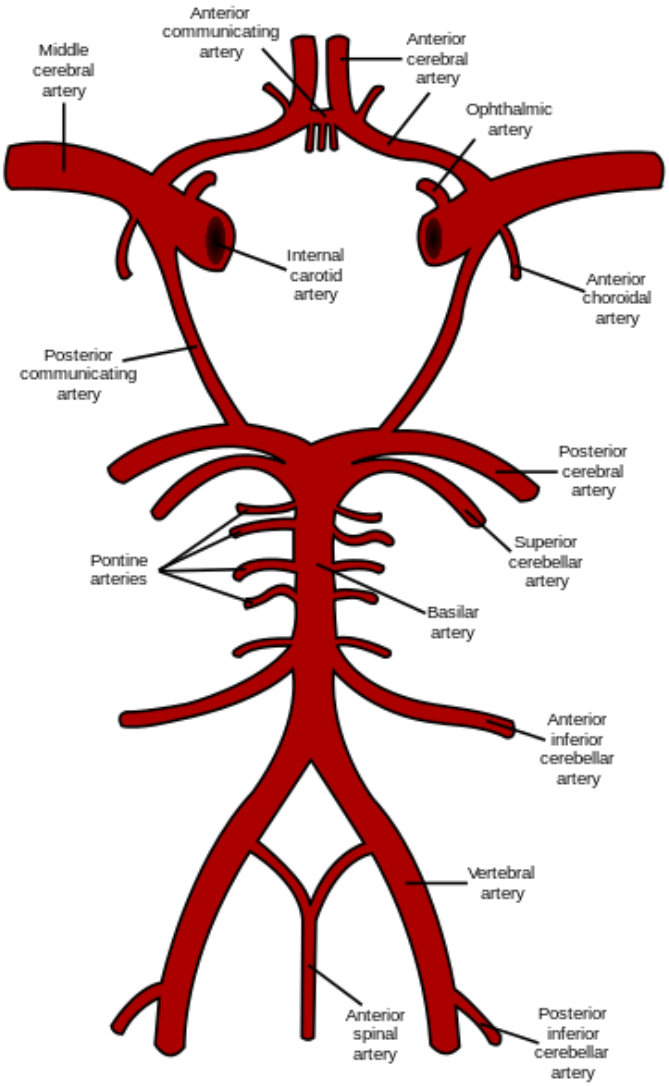

Figure 1-1: The Circle of Willis

The perforators supply blood to the region of the brain called the pons, which is responsible for the control of many base functions including, taste, facial expressions, respiration, and sleep. The AICAs primarily provide blood to the regions affecting hearing and balance. In normal physiology, there are two AICAs and many pontine perforators. The number and location of perforators can vary significantly from person to person, and their location can be further shifted by a change in the basilar artery, such as the formation of an aneurysm.

1.3. **Background – Cerebral Aneurysms**

An aneurysm is an abnormal bulge in an arterial wall. Although their exact cause is not clearly understood, they develop through a combination of abnormal hemodynamic forces and weak arterial walls, generally forming at locations of branching points (1) (2). They can impinge on surrounding tissue, cause thromboemboli, and at times, can rupture, causing hemorrhage.

Due to their location, cerebral aneurysms pose increased risks. Even without the risk of embolism or rupture, the pressure from an enlarged artery can cause other neurological symptoms in the patient (2). Additionally, due to their location, diagnosis and treatment can be difficult, and treatment can often lead to worse outcomes than leaving the aneurysm alone (3). This risk has reduced in recent years (4), due in part to the use of physical modeling and computer simulations. Any improvement in the quality of the models and simulation methods will further reduce these risks.

1.4. **Simulations as a Predictive Tool**

As technology has advanced, it has become reasonable to not only simulate the existing flow patterns but to make modifications to the model to explore different surgical procedures to treat cardiovascular lesions such as aneurysms (5). Simulating surgeries based on actual patient geometry allows a surgeon to plan ahead, selecting the surgical option which will have the greatest chance of success.

1.5. **Limitations of Previous Studies**

By their nature, simulations require the use of assumptions to simplify their scope. Assumptions allow for the faster generation of results and a more focused analysis in an area of

interest. These assumptions can take the form of using only part of a system or taking certain physical phenomena for granted.

In previous simulations of basilar aneurysms, the common practice is to ignore any vasculature too small to significantly impact the flow patterns through the basilar artery (6) (7). If the goal of the study is simply to analyze flow pattern changes near basilar aneurisms due to different surgeries, this is a safe assumption.

Research has shown that, although the overall flow patterns are largely unaffected by the inclusion of this smaller vasculature, the volume of blood reaching this vasculature must also be considered when reviewing surgical options (8). Alterations to the flow patterns to alleviate the aneurysmal symptoms can be unintentionally detrimental to the proper volume of blood reaching the lower regions of the brain.

1.6. **Study Approach**

The smaller arterial branches of the basilar artery are too small to accurately discern from the noise and artifacts inherent to present-day scanning methods (9). Including these in a simulation requires manually adding them to the model. The size and shape of these features can be estimated based on previous research and experience, but they vary in size, quantity and orientation between individuals. The differences in these parameters could cause different flow patterns and flow rates both through these features and throughout the entire basilar artery.

The studies performed in support of this thesis evaluate the sensitivity of several of these parameters. The diameter, length, location and quantity of the manually generated

arteries are each assessed individually by comparing two or more models with the parameter under investigation being the only change.

To determine the impact of these changes on the resulting flow patterns, the results of the studies will compare flow patterns, flow distribution and wall shear stress (WSS) differences among other indicators.

1.7. **Study Limitations**

The studies in this thesis are comparative in nature. The findings demonstrate a trend related to the parametric change such as an increase or decrease in flow rates, changes in flow circulation patterns or WSS differences between simulations performed on two or more variations of a model. This thesis is not intended to match actual performance of the patient or any physical model.

Any assumptions made when setting up the studies should not affect the interpretation of the results. The findings should be valid for a more complex system, so long as the assumptions remain consistent throughout the simulations in each of the studies.

1.8. **Applications**

The primary focus of this thesis is to improve the understanding of the methods currently used to create models for use in blood flow simulations. The methodology given here will allow researchers to make better decisions when creating model geometry, leading to more robust results from their simulations.

Alternatively, the results of these studies can be used as a starting point for more advanced research. With sufficient data, these geometries can be used to fine-tune the simulation to match the flow patterns present in the patient more accurately.

1.9. **Organization of Material**

Chapter 2 reviews previous approaches to the simulation of vascular systems and outlines their methods, conclusions, and limitations. It acts as the foundation for this thesis and helps clarify the purpose of the studies and the reasoning behind much of the methodology.

Chapter 3 outlines the methods of model generation and the approach to the studies. The first section describes the vasculature in this region in a typical person. The second section gives a description of the models used in the simulations, including how the data was acquired and how the models were created. Also defined are assumptions made during the modeling process, any changes, removals or additions to the geometry, and the details and justification of the mesh used for the Computational Fluid Dynamics (CFD) process. Next is an overview of the numerical theory behind the simulation process. The final part of the chapter describes each of the studies, both the models used and the parameters changed for each simulation.

In Chapter 4, the results of the simulations are presented and briefly discussed. The first half of the studies investigates the sensitivity of variations in the four identified geometric factors; length, quantity, diameter, and location of the lateral arteries.

The studies in the second half of Chapter 4 investigate the use of a resistive force applied at specific outlets to adjust the flow patterns.

In Chapter 5, the results of the simulations are discussed, with recommendations for additional studies where the results seem uncertain.

2. Literature Review

2.1. Overview

Technological advances over the years have improved our capabilities for imaging human vasculature as well as modeling and predicting its behavior. With the advent of these tools, as well as improved surgical techniques, surgeries to remedy vascular diseases have a much higher rate of success (10). There are limitations with the methods, and there is always room for improvement.

It is essentially impossible to match human vascular performance in a simulation perfectly, so it is up to the researcher to determine what is necessary to their study and make appropriate assumptions to allow for a more focused study. It is important to learn from previous research, to determine which assumptions can be made and which aspects can be omitted when performing any new investigation.

This chapter is a review of previous analysis and simulation of basilar aneurysms and similar vasculature. The literature selected establishes a timeline of various approaches leading up to the current methodologies. These previous studies give reasoning behind the methods and assumptions used in the studies performed in this thesis.

2.2. Aneurysms

2.2.1. Cerebral Aneurysms

Cerebral aneurysms can be grouped into three categories: saccular, fusiform and lateral. Saccular aneurysms are the most common; typically forming at the bifurcation of a “Y” junction in the vasculature, most often at the base of the brain. They take the form of a pouch-like sac, with a narrow “stem” where they attach to the artery.

Fusiform aneurysms present themselves as an overall swelling of the artery in all directions. They seldom rupture but may impinge on surrounding tissue.

Lateral aneurysms appear as a bulge on one side of the blood vessel, more localized than a fusiform aneurysm but without the formation of the sac present in a saccular aneurysm. They tend to form at locations of arterial curvature rather than branches. Lateral aneurysms are often identified as a subset of fusiform aneurysms (11).

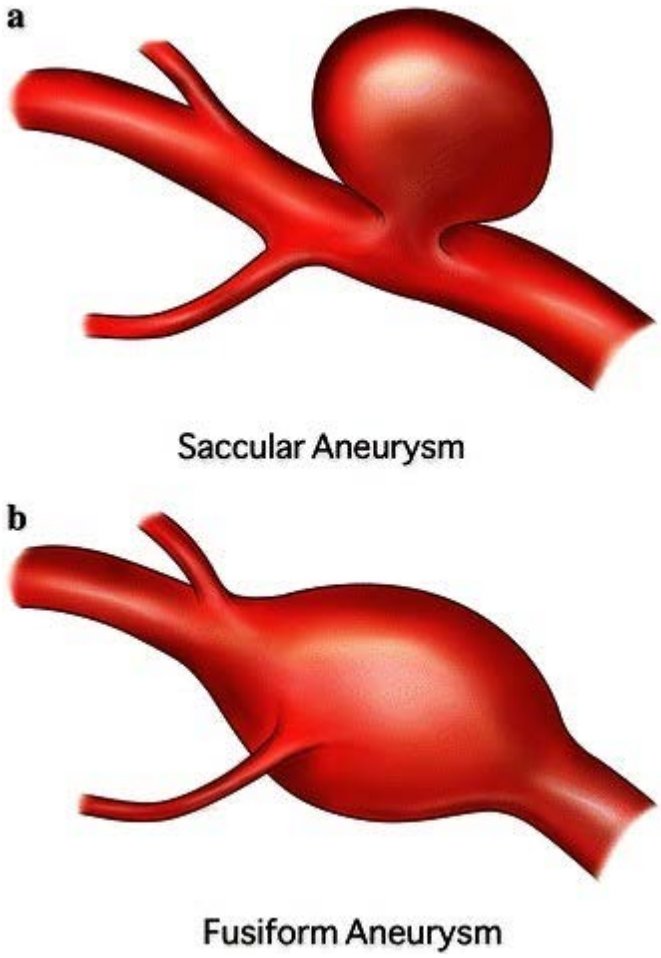

Figure 2-1: Saccular and Fusiform Aneurysm

Approximately 10% of cerebral aneurysms develop in the region of the basilar artery. The majority of these can be found in the basilar artery itself rather than in any of the branching vessels (12).

2.2.2. **Surgeries**

There are several general approaches to aneurysm treatment; coiling, clipping, stenting and bypass surgery are common (12). Most of these are well suited for treating saccular aneurysms. In the case of fusiform aneurysms, clipping is the preferred surgical method, but bypass surgery is an option when an aneurysm cannot be clipped without affecting the distal flow.

Due to the sensitive location and small lateral branches, aneurysms in the basilar artery are particularly difficult to treat. Care must be taken with any procedure to avoid compromising flow to the brain stem. Standard clipping procedures tend to restrict the flow significantly, so flow bypass procedures are often used instead (13).

The goal of bypass surgeries is to reduce the blood flow through the aneurysmal vessel, with the intent of inhibiting the progression of the disease. With restricted flow, a protective layer of thrombus will form, slowing or even stopping the future growth of an aneurysm. These procedures alter the blood flow patterns, either by decreasing the number of outlet arteries or by changing the flow direction entirely. It is crucial that any new flow pattern supplies sufficient blood to the vessels in the basilar region and that the resulting thrombus does not obstruct flow to the brainstem perforators.

Any treatment carries a risk of worsening the condition of the patient, so it is best to only attempt treatment on patients with the highest risk of aneurysm rupture (14).

2.2.2.1. Simulation Methods

Before the 1990s, most investigations into cerebral aneurysms and their development had been conducted post-mortem, but modern advances in imaging technology have allowed us to gain a better understanding of these lesions and make progress in their diagnostics and treatment.

2.2.3. Numerical Study of Cerebral Vasculature

The human vascular system can, in broad terms, be described as a complex system of pipes. The pipes work as a distribution network, branching in a pattern can be approximated by a bifurcating fractal tree system (15). Because of this, the earliest examinations of the vascular system were performed using flow theory described by Bernoulli, Poiseuille and the Navier-Stokes equations which were developed for general purpose fluid dynamics calculations. The use of such equations in their basic form assumes rigid vessel walls, Newtonian behavior of blood, and ignores the pulsatile nature of blood flow.

In large arteries, the vessel size is sufficiently greater than that of the blood cells so using a non-Newtonian fluid model is a safe assumption. In smaller vasculature, the cells are large enough relative to vessel size to affect the fluid properties, and viscous effects begin to gain dominance over the flow behavior. The non-Newtonian nature of blood starts to become significant at this scale.

The pulsatile nature of blood flow is less apparent in smaller vasculature than in larger vessels, so can more easily be ignored when using these equations at a smaller scale.

In the 1950s, Womersley performed studies using elastic tubing to simulate vasculature (16). The purpose was to try to emulate blood flow using a flexible tube wall. The results of his research showed that when simulating a region of vasculature, numerical factors could be applied to the outlets which would emulate an elastic response to inlet pressure from any downstream arteries. His research led to the Womersley Number, which is used to compare the pulsatile frequency with the viscous effects in blood flow. His work was one of the first analytical models for the study of biofluids.

Building on this initial work, several ensuing studies (17) assumed a constant resistance, in the form of a distal pressure, applied at the model outlets. The term distal pressure is used to describe a pressure which represents the resistive force of downstream features. A constant resistance assumes the pulse frequency and downstream conditions to be in phase, which is not the case in larger arteries. This approach is, however, valid in smaller arteries.

Olufsen (18) demonstrated that the effect of downstream vasculature should instead be emulated as impedance rather than a static value. This work still assumes an elastic behavior of the arterial walls but also accounts for the pulsatile behavior of the flow which had not been addressed in earlier work.

The work by Vignon-Clementel et al. (15) shows using impedance is far more accurate, but requires 6 or more cardiac cycles to establish a periodic solution, while the solution using a constant pressure becomes periodic within 2 cycles. Generating an accurate impedance model requires direct data from the patient or a complex model to estimate of the downstream vasculature.

The constant pressure approach is used for the simulations in this thesis. In regions of very small vasculature, where the downstream branches transition into capillary flow, the use of a constant pressure gives reasonable results.

2.2.4. **Physical Models of Aneurysms**

The earliest approach to the simulation of flow behavior in the cerebral vasculature was the use of physical models. Constructing approximate models from tubing and other components has been performed since the 1950s. These models had their limitations and were primarily intended to replicate idealized, healthy patient physiology. There is significant variation among patients with aberrant vasculature, such as an aneurysm, so it becomes impossible to create a predictive model which would work in all situations. Actual patient models are required to study the blood flow patterns through aneurysms.

The initial approach to this type of model creation is to make a cast of the patient's vasculature post-mortem and create a model using a polymer. The polymer used was based on the phenomena being studied. If the elasticity of the vasculature is a significant factor, the model would be made of an elastomer. An example of such a simulation is described in the paper by Chong et al. (19). In studies where the visualization of flow patterns is important, the researchers use a transparent resin, which allows for a tracer agent or other method to be utilized to observe swirling and stagnation in the model. An example of a study using such an approach is the research performed by Imbesi and Kerber (20).

Although useful to study the flow patterns in aneurysms in general, these models are limited in that they pertain to one single patient, who is already deceased. More casts can be

made to get a wider range of sampling, but given that every patient has significantly different vasculature, this would still have limited use.

The ideal situation would be to get the exact geometry for the patient to be treated while they are still alive, which requires better tools for acquiring such geometry without adversely affecting the patient.

2.2.5. Imaging Methods

Many imaging methods have been used to analyze cerebral vasculature over the years, which are discussed at length by others (21). Presently, the most common methods used for imaging of these types of lesions are computed tomography angiography (CTA) and Magnetic Resonance (MR).

There are several MR methods, each targeted toward a specific tissue or fluid. MR angiography (MRA) is used to evaluate blood vessel geometry. Standard MRA methods are not ideal for to determine fluid flow behavior, so a phase-contrast magnetic resonance imaging (PC-MRI) method is used for the transient data.

Due to their small size, the lateral branches of the basilar artery are not accurately represented in these images. Higher resolution angiography and 3D rotational techniques are being investigated to improve the ability to capture these geometries, but even these are limited in what they can render (9).

2.2.6. Computer Modeling and Simulation

By the early 1990s (22), computers and imaging technologies had advanced sufficiently to allow researchers to perform computer simulations.

These early studies (23) made a point of highlighting the limitations of tools of the time. From a modeling standpoint, transient flow data was difficult to obtain with the imaging methods at that time, so flow data from patients with similar physiologies was used. For the simulations themselves, the limiting factor was often computational power, forcing the researchers to simplify their models. These first models consisted of simple cylinders and straight tubes. The over-simplified models tended to underestimate the WSS and oversimplify the flow patterns (24)

By the 2000s, imaging technologies and computational capabilities had both advanced sufficiently to allow for simulations with patient geometry derived in vivo (23). The imaging process benefitted from the use of improved methods in rotational angiography. A series of 2D scans could be performed on a patient at set distances from each other. These "slices" could then be combined into a 3D version of the scan in a process known as Image-Based Modeling. As early as 2003, researchers have been able to perform simulations using geometry based on actual patient scans taken in vivo (23). The ability to transition from patient scans to a 3D model started a shift from computer simulation being used primarily for research towards its use to diagnose and treat living patients (25).

For the first time, the results from computer simulations could be compared with direct angiographic imaging (26). The results were positive, showing an accurate representation of complex flow structures.

2.2.7. **Improved Capabilities**

In more recent years, the capabilities of both imaging technologies and simulations tools continue to improve dramatically, allowing for a more accurate use of CFD as a tool for diagnosing and treating cerebral aneurysms (10) (27).

With the advent of high-quality rapid prototyping technology, the capability of making physical models has also improved. These models can be used to compare the results from computer simulation to a physical representation (28) (29) (30), allowing for more confidence in the results of both.

New methods of medical imaging are also being investigated to improve the quality of what data can be acquired from the patient, with higher resolution (9) and more accurate determination of velocity and flow patterns (31) being researched. The implementation of the data from these new techniques will improve the quality of the simulations over time.

2.3. **Summary**

The work reviewed in this chapter gives an overview of the physiology involved and provide both a background into the study of the simulation of basilar arteries, and provide precedent for many of the assumptions made in the following chapters.

3. Study Development: Theory, Modeling, and Simulation Procedure

3.1. Introduction

This chapter offers an overview of the physiology of the area of the study, a description of the models and model construction, the numerical theory used in the solution methods and a description of the studies performed. The studies themselves and their results will be described in the next two chapters.

Section 3.2 describes the specific details of the anatomy of the basilar artery, building off of the broad overview in Section 1.2. The background for the determination of the size and location of the added geometry is given, and any assumptions made to simplify the simulations are defined.

Section 3.3 describes the patient geometries used in the simulations as well as the methods employed to create the models and generate the model meshes.

Section 3.4 begins with the mathematical background for CFD and then describes how the ANSYS software is configured based on this mathematical theory and how it applies to these simulations.

The chapter finishes with section 3.5, which gives an overview of each study. In each case, it specifies which model and model versions are used, the parameters being investigated, and any additional settings specific to that study.

3.2. Physiology

3.2.1. Blood Vessel Data

Table 3-1 lists the size ranges typically seen in the vasculature being analyzed in this study as well as the general sizes of some typical vasculature for reference (32) (33) (34) (35).

The information from this table is used as a rough guideline for creating the user-made geometry in the models.

Table 3-1: Geometries of Typical Vascular Features

Feature	Diameter (mm unless noted)	
	Average	S. D.
Capillaries (for scale)	*0.005*	-
Red Blood Cell (for scale)	*0.007*	-
Length of Basilar Artery	29.9	0.29
Diameter of Basilar Artery	3.59	0.38
Vertebral Artery (left)	3.23	0.57
Vertebral Artery (right)	2.95	0.47
AICA	1.26	0.43
SCA	1.56	0.44
PCA	2.52	0.36
Perforators (dia)	0.282	*(not available)*
Perforators (qty) Left	4.8	0.83
Perforators (qty) Right	4.5	0.75
Perforators (qty) Total	9.2	1.19

Referencing Figure 1-1, the primary arteries of interest in this thesis are the vertebral arteries, the PCAs, the SCAs, the AICAs and the perforators. Note that the total quantity of perforators is typically in the range of 20, but the study used for that data only accounted for perforators above a certain size. (33)

For several of the studies, the target performance is based on the ratio between the blood exiting the apex and that exiting the lateral branches. This ratio can be estimated for a specific patient by determining the flow at the inlets (VAs) and the apex outlets. However, the apex flow data corresponding to the models used in this thesis was not acquired from MRI data, so typical values are used instead.

Zarrinkoob et al. (36) performed an analysis of blood flow distribution throughout the entire network of cerebral arteries, using both typical and aberrant physiologies for comparison. Table 3-2 summarizes a subset of the data related to the region of the basilar artery. The smaller physiology is not addressed directly within the paper, but can be inferred from the data by making several assumptions: 1) The entirety of the blood flow through the PCAs comes through the basilar artery, rather than from other arteries supplying the Circle of Willis, 2) any other smaller arteries which are not present in Figure 1-1 do not exist and are not accounted for, and 3) the "lost" flow rate in the upper portion of the basilar artery goes entirely through the SCAs. As they are not intended results of the Zarrinkoob study, these values have a high level of uncertainty but are sufficient to give a general idea of how much of the inlet flow

Table 3-2: Typical Blood Flow Rate Distribution

Feature	Flow Volume (mL/min)		
	Average	Percentage of Total Flow	S. D.
Inlets			
Right Vertebral Artery	100	50.0%	48
Left Vertebral Artery	100	50.0%	48
Total VA	200	100.0%	67.9
Outlets			
Basilar Artery	145	72.5%	41
Right PCA	54	27.0%	12
Left PCA	54	27.0%	12
Calculated			
Lateral Artery "Loss" (AICAs/Perforators)	55	27.5%	79.3
Apex Artery "Loss" (SCAs)	37	18.5%	44.4

should go towards the lateral branches.

The result of these calculations shows approximately 72.5% the flow entering through the vertebral arteries exiting through the PCAs and SCAs, leaving the remaining 27.5% to exit through the AICAs and perforators.

Based on communications from Professor Rayz, this ratio typically falls within the range of 80%/20% to 90%/10% ratios. The 90%/10% ratio was selected as the worst-case condition.

3.2.2. Assumptions

To aid in the analysis of complex anatomy such as this, it helps to simplify the process by making certain assumptions about the model or the conditions (37).

- **Blood is assumed to be a Newtonian, incompressible fluid**. Several studies (7) (38) have shown that using a Newtonian model for blood has little effect on overall flow patterns and WSS in such simulations. The properties of the blood used in this study are as follows: Fluid type: liquid, Density: 1060 kg/m^3, Viscosity: 0.0035 kg/m-s (39).
- **The walls are rigid**. Using rigid walls, particularly in the basilar artery where there is little room for vessel walls to pulsate, is a safe assumption and makes the simulations much easier. Aneurysmal disease causes an additional loss of wall elasticity, making a rigid wall assumption even more reasonable (31). Previous studies (1) have shown that while allowing for wall flexibility will change velocity magnitudes and WSS, flow patterns are not significantly altered.
- **Downstream pressure is constant.** This assumption is closely related to the rigid walls assumption listed previously. As mentioned in Section 2.2, many studies have been performed on the pulsatile nature of the distal pressure on blood flow due to the

downstream elasticity. However, following the same reasoning used in the rigid walls assumption, the pressure pulsation should not be significant to this study.

- **The patients in this study have normal anatomy.** Aside from the aneurysm; the size and shape of the generated anatomy (AICAs and perforators) are based roughly on the data from Table 3-1, which assumes average values for the features. This assumption also includes the AICAs having nearly the same diameter and length as each other and the perforators each having the same diameter and length as each other. A normal anatomy also means that the blood flow distribution will follow what is shown in Table 3-2.
- **Approximately 90% of the flow entering the basilar artery exits the PCAs and SCAs; the other 10% exits the AICAs and perforators**. The 90%/10% assumption was used as a baseline of "normal" to help establish and verify data in several of the studies. There is enough variability in physiologies (36), and there is a large enough quantity of smaller lateral branches that it becomes difficult to get an exact measure of a "typical" flow ratio through these arteries.
- **Cardiac cycles repeat identically.** A portion of the patient data used in these studies is transient flow velocity data at the vertebral arteries. This data is taken over a single cardiac cycle. For simulations run for more than a single cardiac cycle, the assumption is that this flow velocity pattern is identical in all cycles. Since cardiac cycles are typically very similar, particularly when measured sequentially, this is a safe assumption.
- **General assumptions**. For overall simplification of the simulations, there are several general assumptions. Most of these are rather obvious but are noted here for the

purpose of repeatability. These include: no gravitational effects, constant temperature throughout the study, no embolisms or other obstructions in the arteries other than what was apparent on the patient scan, and blood cells and other suspended solids are too small to significantly alter the flow in this study, based on the data in Table 3-1.

3.3. **Models**

A note on the convention of orientation naming: for any part of human anatomy, the notions of "left" and "right" are oriented per the standard anatomical position; i.e. the point of view of the patient. The models used in this simulation are shown viewed from the anterior allowing for a less obstructed view of the physiology for analysis but reverses these directions in the images. Therefore, throughout the descriptions of the models and discussions of the studies, "left" and "right" will be correctly oriented for the anatomy, but will be reversed from the location in the images themselves.

3.3.1. **Model Information**

Two patients presenting basilar aneurysms were imaged and treated at the UC San Francisco, their imaging data used in these simulations. In both cases, the aneurysms were unsuitable for clipping or coiling and thus considered for a surgery altering the pathological blood flow patterns. For each patient, two versions, representing the flow resulting from different surgical procedures, were modeled. Variations to the geometries performed as part of the studies, such as perforator quantity or size, are described in section 3.5. To preserve the anonymity of the patients, they will be referred to as "patient 1" and "patient 2".

For patient 1, two models were created, each representing the result of a different surgery intended to treat the aneurysm.

Figure 3-1 depicts the first of the two; the Patient 1 “bypass” surgical option, where the top portion of the basilar artery is severed. The model represents the post-operative flow following a clipping of the basilar apex with a bypass as shown. The right PCA, left PCA, and left SCA are uninvolved in the simulations, being part of the bypass system. The flow being investigated enters through the vertebral arteries with the only apex artery in use being the right SCA. The purpose of this surgery is to restrict the overall flow rate through the basilar artery while the resistance caused by the single apex outlet should maintain the flow to the lateral branches.

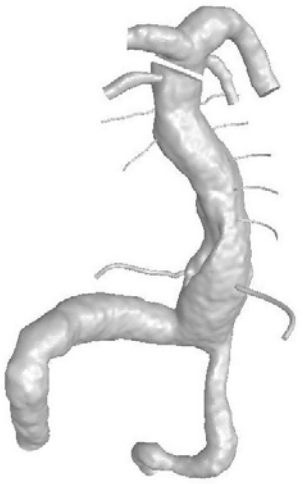

Figure 3-1: Patient 1 “bypass” Geometry

There are two perforators modeled near the top of the right side, near the right SCA, and five perforators on the left, evenly spaced. They are of uniform diameter and nearly equal length. A large thrombus mass was observed on the right side of the basilar trunk; thus the perforators adjacent to the thrombus location were excluded from the model.

The second model is the Patient 1 “sump” model, depicted in Figure 3-2. For this option, the apex portion of the basilar artery was left intact. The proximal part, where the

vertebral arteries would normally merge into the basilar artery, was removed and capped off, approximating the result of using a surgical clip. The flow from the vertebral arteries was rerouted to the right PCA which causes the blood to be supplied to the AICAs and perforators in a retrograde fashion. This surgery also intends to reduce overall flow through the basilar artery but may compromise the blood supply to the lateral branches as a result.

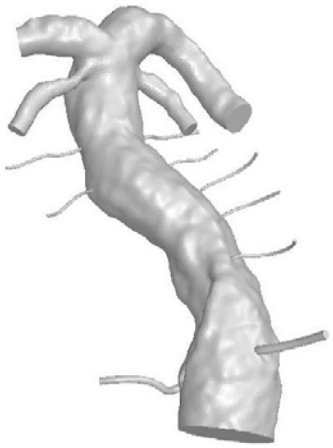

Figure 3-2: Patient 1 "sump" Geometry

The AICAs and perforators are identical to those of the "bypass" version of the model, which allows for a more consistent data comparison.

Two versions of the patient 2 model were also used in the simulations. The first is a preoperative version, denoted as Patient 2 "preop" depicted in Figure 3-3.

This model has 13 total perforators, six on the right side and seven on the left side. They are approximately evenly spaced and of roughly equal length. This model is the primary one used in studies relating to changes due to adjustments in size, shape, and location of the perforators. The version depicted in Figure 3-3 is the "base" model for those studies.

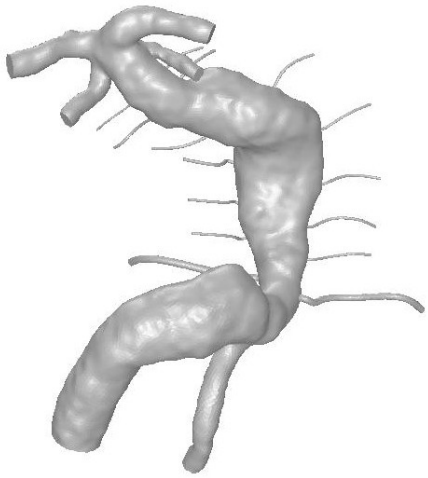

Figure 3-3: Patient 2 "preop" Geometry

The second version of the patient 2 geometry is a "sump" model, depicted in Figure 3-4. This model represents the same surgical procedure as was used in the Patient 1 "sump" model version. The right PCA is used here as the flow inlet as well.

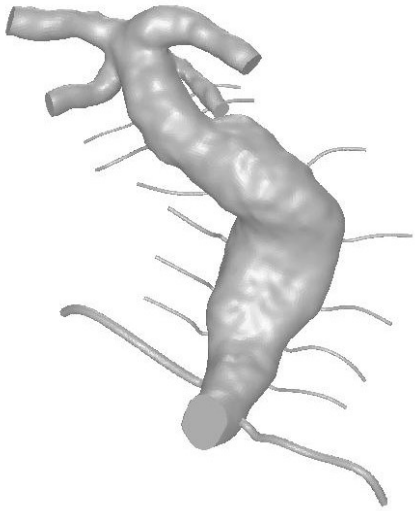

Figure 3-4: Patient 2 "sump" Geometry

This model retains the same quantity and lengths of the perforators and AICAs as the preoperative version.

3.3.2. **Model Generation**

The models used in this study were generated using high-resolution Contrast Enhanced MRA (CE-MRA) data from the two patients. An example 2D image is shown in Figure 3-5. The output files from the CE-MRA process are in the form of a series of thin 2-D slices which can be rendered into a 3-D object using image-based modeling (40).

Figure 3-5: 2D MRA Example

The vessel geometries in this study were modeled using Geomagic software. The contrast-enhanced images of the vasculature can be selected within the software and output as a 3-D surface model. The quality of the objects created by this process is limited both by the resolution of the 2-D imaging technology, and the size of the gap between the slices. The software interpolates the information between the slices, but any vasculature similar in scale to or smaller than the resolution is lost in the rendering process. Likewise, some of the smaller vasculature and other "noise" showing up in the 2-D images often becomes extrapolated by the software, creating a rough surface and thin, jagged tendrils, which must be removed.

The process of cleaning up the model is performed manually using Geomagic software. It involves first removing any vasculature which is outside of the scope of this study. Next, artifacts from the imaging process are removed. As a final step, the overall surface is smoothed using a surfacing tool, while still keeping as much of the geometry intact. These steps must be performed carefully; which geometry should be saved and which is just a remnant from the scanning process is based on knowledge and experience of how this vasculature should appear. The output from this process is a 3-D shell model in either .STL or .IGS format.

The model is further prepared using Altair Hypermesh. Using the typical sizes and quantities for these features as described in Table 3-1, the left AICA, right AICA, and several perforators are created. The features are designed to have relatively uniform diameters and lengths and are curved to reflect typical brainstem geometry.

Surface features, or "caps" are created where each of these added geometries merges with the wall of the basilar artery. These caps allow for greater control over the use of these geometries during the simulations. During a flow simulation using the entire geometry, these caps are set to be internal features, which do not block or otherwise affect the flow. If the simulation requires one or more of the perforators or AICAs to be absent, the cap can be changed into a "wall" feature, restricting blood flow to that outlet.

The lengths of the modeled features are far shorter than what is present in physiology, which is also the case with the PCAs and SCAs. Part of the intent of this research is to determine a suitable length to model these features, but for the purpose of creating the models for this thesis, the lengths of these arteries are roughly estimated, the value tracked for comparison with the results.

3.3.3. **Model Meshing**

The next step in model creation is to create the mesh of elements used in CFD simulation, which was performed using Altair Hypermesh. The mesh was generated by first creating a 2-D surface mesh, then extending a 3-D mesh into the models from the surface elements.

Below a certain optimal mesh size (7), the overall flow characteristics will show little or no improvement as the mesh is further refined. The goal is to use an element size that is large enough to simplify calculations within the large regions, yet small enough in the smallest flow conduits to resolve WSS effects (41) (42) accurately.

The mesh was configured manually, generated from a set of user-entered criteria, to better control the focus to specific regions of the models.

Element selection was varied between the models as part of a side study investigating the effect on computation time. Quadrilateral/prism meshes converge quicker than other element types and give more accurate results, but are difficult to use in models that are not constructed of uniform geometries. Simple triangular/tetrahedral meshes tend to fit more easily into irregular-shaped bodies, but they give the least accurate results. More complex triangular/tetrahedral elements, with additional nodes along the edges, offer the shape benefits of their simpler counterparts, but with a much greater accuracy. However, they have the longest time to convergence during simulation.

After an initial comparison of a model using a complex tetrahedral mesh and one with mixed prism/tetrahedral elements, the combination mesh offered a faster computation time with no discernable difference in flow results. Typically, adding an inflation layer mesh to the

walls of any tube-like fluid conduit is recommended (42), but the twisting nature of these outlets caused element discontinuities with this approach. Given the small artery size and laminar flow regime, a highly structured inflation layer is not required for accurate results.

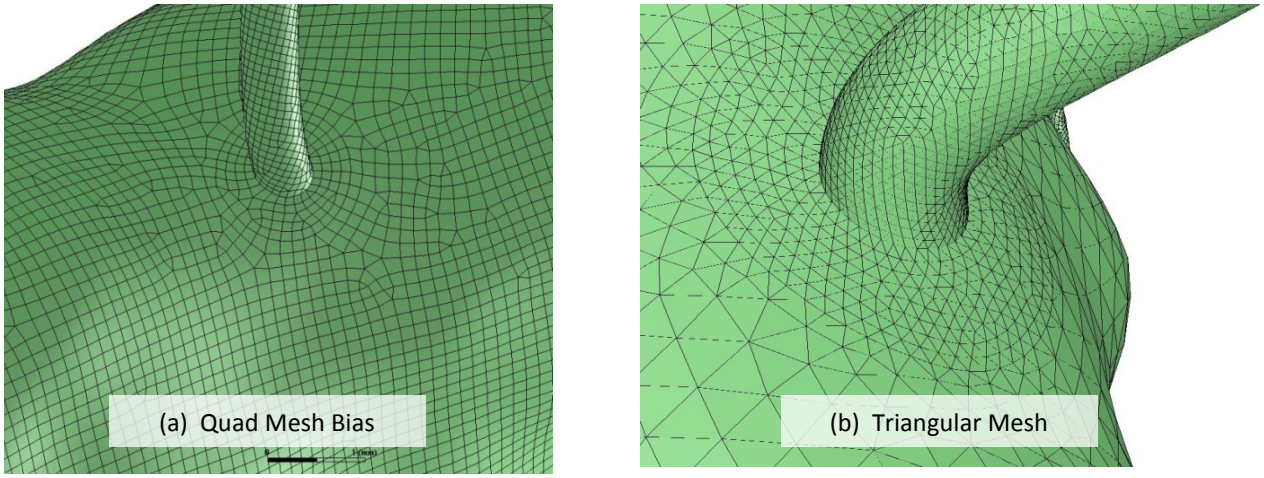

Figure 3-6: Mesh Examples

The trunk of the basilar artery, the vertebral arteries, and the apex arteries were meshed using a 0.30 mm mesh size. The walls of lateral arteries were meshed using a 0.07 mm element size. Circular regions were added where the AICAs and perforators join with basilar artery and given a 0.12 mm mesh density. Figure 3-6 shows the results of some of the meshing activities where the three mesh density regions can be seen. The size of these transition zones was somewhat arbitrary, but they were drawn to be approximately three times the diameter of the outlet attached at that location. Figure 3-6(a) shows one which has a quadrilateral mesh bias while Figure 3-6(b); represents the mesh created entirely with complex tetrahedral elements.

Figure 3-7 shows the end detail of one of the smaller perforator outlets as an example of the resolution of the elements in these features.

The number of elements in the models for each simulation is shown in section 3.5.3

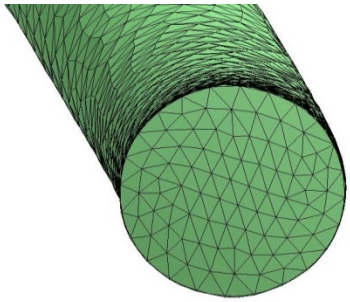

Figure 3-7: Outlet Mesh Detail

3.3.4. Transient Data

Inflow waveforms obtained from PC-MRI data are prescribed at the model inlets to simulate the flow through the cardiac cycle. The transient data is imported into ANSYS for use in the simulations. The data is consists of a number of time steps, the size of each step in seconds, and the velocity at the inlet(s) in meters per second at each time step. Each data table represents one full cardiac cycle for the patient.

There are three sets of transient data for Patient 1: “postoperative”, “reimplanted SCA” and “AICA sump 1”. Each data set consists of 32 steps with a size of 0.025 seconds each, for a total of 0.775 seconds for the cardiac cycle.

There are two sets of transient data for Patient 2: “preoperative” and “AICA Sump 2”. Each data set consists of 32 steps with a size of 0.016 seconds each, for a total of 0.496 seconds for the cardiac cycle.

Figure 3-8 shows one of the transient data sets. The two inlet velocities are kept separate rather than combining them and starting the simulations above where the vertebral arteries merge, allowing the simulations to properly track any mixing behavior of the two flow streams (6).

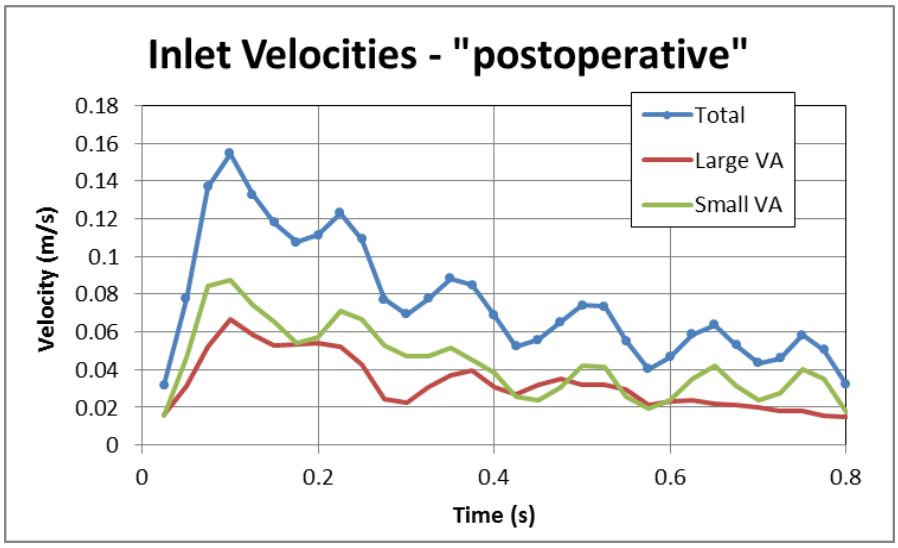

Figure 3-8: Transient Data Example

3.4. Simulation Methods

3.4.1. Numerical Theory

The mathematical models used in CFD computation are based on the Navier-Stokes equations (43). The Navier-Stokes equations consist of a set of partial differential equations (PDAs) which describe the velocity and pressure fields. They are shown here for reference:

Assumptions:

- The effect of gravity is negligible: $\rho g = 0$
- Fluid is incompressible

Continuity Equation:

$$\frac{\partial}{\partial x}u + \frac{\partial}{\partial y}v + \frac{\partial}{\partial z}w = 0 \quad \textbf{(3-1)}$$

Momentum Equations:

$$\hat{x} \rightarrow \rho\left[\frac{\partial u}{\partial t} + u\frac{\partial u}{\partial x} + v\frac{\partial u}{\partial y} + w\frac{\partial u}{\partial z}\right] = -\frac{\partial P}{\partial x} + \mu\left(\frac{\partial^2 u}{\partial x^2} + \frac{\partial^2 u}{\partial y^2} + \frac{\partial^2 u}{\partial z^2}\right) \quad \textbf{(3-2)}$$

$$\hat{y} \rightarrow \rho\left[\frac{\partial v}{\partial t} + u\frac{\partial v}{\partial x} + v\frac{\partial v}{\partial y} + w\frac{\partial v}{\partial z}\right] = -\frac{\partial P}{\partial y} + \mu\left(\frac{\partial^2 v}{\partial x^2} + \frac{\partial^2 v}{\partial y^2} + \frac{\partial^2 v}{\partial z^2}\right) \quad \textbf{(3-3)}$$

$$\hat{z} \rightarrow \rho\left[\frac{\partial w}{\partial t} + u\frac{\partial w}{\partial x} + v\frac{\partial w}{\partial y} + w\frac{\partial w}{\partial z}\right] = -\frac{\partial P}{\partial z} + \mu\left(\frac{\partial^2 w}{\partial x^2} + \frac{\partial^2 w}{\partial y^2} + \frac{\partial^2 w}{\partial z^2}\right) \quad \textbf{(3-4)}$$

The terms of the momentum equations can be broken up into their individual components. Using the $\hat{z}$ component of the equation set, Equation ((3-4), as an example, the following components make up the momentum equation in the z direction.

$$\rho\frac{\partial w}{\partial t} = temporal\ acceleration\ term \quad \textbf{(3-5)}$$

$$\rho\left(u\frac{\partial w}{\partial x} + v\frac{\partial w}{\partial y} + w\frac{\partial w}{\partial z}\right) = convection\ term \quad \textbf{(3-6)}$$

$$-\frac{\partial P}{\partial z} = Pressure\ gradient \quad \textbf{(3-7)}$$

$$\mu\left(\frac{\partial^2 w}{\partial x^2} + \frac{\partial^2 w}{\partial y^2} + \frac{\partial^2 w}{\partial z^2}\right) = Viscous\ Effects \quad \textbf{(3-8)}$$

This set of equations is used to calculate the velocity field for each element in the mesh. There is no analytical solution to the Navier-Stokes equations for flow in realistic vascular geometries (44), so it is approximated using one of the various numerical schemes. Most of

these schemes rely on the flow field in the adjacent elements, which requires solving a system of interrelated equations, requiring either an iterative or simultaneous solving method.

When using the ANSYS Fluent software to perform CFD, various options may be selected to establish which numerical schemes are used to determine these results. Higher order methods will use more nearby elements for more accurate computation. Other parameters control the iterative methods and the convergence criteria. The numerical schemes selected for these simulations are outlined and described in section 3.4.3.

3.4.2. **Fluent Settings**

The simulations were performed in ANSYS Fluent software, initial studies in version 14.5.7 and some final studies using version 17.0. The models created in Hypermesh were imported into the Fluent CFD software.

Many Fluent settings are constant throughout all of the simulations. The general settings are listed here to enable replication of the results. The numerical schemes selected for solving the Navier-Stokes formulations are described in the following sections.

- Solver Type: Pressure-Based
- Velocity Formulation: Absolute
- Time: Transient
- Gravity: No
- Models: Viscous-Laminar

3.4.3. **Numerical Schemes**

In configuring the simulations, ANSYS Fluent allows the user to select from several options of numerical schemes to solve the Navier-Stokes equations. ANSYS has several guides

thoroughly describing these schemes (45) (46). The schemes selected for these simulations are listed here with a brief description of their formulation and how they apply to the simulations in this study.

3.4.3.1. Pressure-Velocity Coupling

A Coupled Algorithm is selected to resolve the pressure-velocity coupling. As described in section 3.4.1, the pressure and velocity portions of the Navier-Stokes equations are reliant on each other, requiring a "coupled" method to resolve them. They can be solved in an iterative fashion; with calculations solving one followed by the other until they reach equilibrium, or they can be coupled; solved simultaneously in a single matrix. A fully coupled approach takes more simulation time per iteration and requires more computer memory but converges faster.

3.4.3.2. Spatial Discretization: Gradient

A gradient must be determined for each element to allow for higher order computational schemes to be used. For these simulations, a "Least Squares Cell-Based" method is selected.

The least squares method uses a linear numerical method, conceptually similar to the "least squares" linear curve fitting method from statistics, to find a weighted average of each centroid's gradient using information from the neighboring cells.

This method is optimal on polyhedral meshes but gives increased accuracy for all meshes in exchange for decreased stability of the simulation. Initial simulations were observed for any stability issues, which were not apparent, so the method was used in all ensuing simulations.

3.4.3.3. Spatial Discretization: Pressure

A second order scheme is selected for pressure discretization. The simplest of numerical schemes: first order, assumes the entire upwind element to have uniform properties as determined at the face in contact with the element being calculated.

In a second order scheme, the calculation uses the same information as the first order scheme, but also includes both the displacement vector and gradient of the upwind elements. This method is more accurate, particularly in a transient simulation, but increases simulation time.

Given the complex geometry of the models and the use of transient simulation methods, the improved accuracy of the second-order scheme is favorable.

3.4.3.4. Spatial Discretization: Momentum

For momentum, a third-order MUSCL scheme is used. The MUSCL scheme (Monotone Upstream-Centered Schemes for Conservation Laws) was conceived as an optimal method for improving on the second-order schemes (47). The method builds on the second-order upwind scheme by including a central differencing method rather than using the values from the adjacent elements directly, resulting in a gradual transition of values between elements, "softening" the results.

In addition to increasing the accuracy, the central differencing scheme also acts to reduce numerical diffusion making it ideal for the simulation of biological systems with complex geometries such as the ones in this study.

3.4.3.5. User Defined Scalar (UDS)

One of the studies requires the use of a user defined scalar (UDS). This feature is used to simulate the advection of a passive tracer agent through the system with what is essentially a hypothetical dye or other substance in the fluid. The inlets were set with an initial value of "1", and each of the outlets was set to "0". During the simulation, the concentration of the tracer agent would be transported by the flow through the system towards the outlets. The results display levels of concentration, showing the filling and wash-out patterns.

The UDS is calculated using the same third-order MUSCL scheme as used for the momentum determination.

3.4.3.6. Transient Formulation

The transient formulation used is a second-order implicit method. A first order time discretization method looks at the previous step, while a second order method looks at the previous two steps, which requires more memory storage during the simulation, but allows for a more accurate transition through the time steps.

3.4.4. Simulation Settings

3.4.4.1. Materials

The wall features of the models are set to "aluminum" to create rigid walls for the simulation. A more detailed discussion of the use of rigid walls can be found in section 3.2.2.

The fluid is set to "blood" with an approximation of blood properties and assuming a Newtonian fluid. See section 3.2.2 for the properties and assumptions used.

3.4.4.2. Boundary Conditions

"No slip" conditions were prescribed at the walls of the model. The outlets for each simulation were set to the "pressure-outlet" option. They were assigned constant gauge pressure of 0 Pa unless otherwise specified in the study. The inlets were set to the "velocity-inlet" option. An initial gauge pressure of 0 Pa was used, which was not changed in any of the simulations. The velocity magnitude was specified using the transient data table.

3.4.4.3. Calculation Activities

Listed below are the settings for how ANSYS handles the iteration procedure. These settings have a smaller impact on the results of the simulations than settings described in the previous sections but are included here for reference.

- Flow Courant Number: 200
- Explicit Relaxation Factors: 0.75 for Momentum and Pressure
- Solution Initialization: Standard Initialization
- Reference Frame: Relative to Cell Zone
- Max Iterations Per Time Step: 200
- Time Stepping Method: Fixed

The number of time steps and time step size varies with the transient data and is described in section 3.5.

3.4.4.4. Outputs

Output monitors are assigned each of the outlets to track mass flow rate in kg/s for each time step. Results are imported into Microsoft Excel for analysis of the flow distribution.

Visual results: streamlines, WSS and UDS analysis, are created using the ANSYS CFD Post software.

3.5. Description of Studies

3.5.1. Geometry Changes

The first group of studies is an investigation of the impact of alterations to the geometry of the basilar side branches: AICAs and perforators.

All simulations described in this section use a single 32 time-step cardiac cycle. Mass flow rate data is taken as an average of the data from all 32 time steps. Flow streamline and WSS analysis are performed on the results from the final time step of the simulations.

3.5.1.1. AICA Length: Patient 1 Bypass Model

This study investigates the flow resistance caused by different lengths of the AICA outlets by comparing two versions of the Patient 1 Bypass model. The first version used the model as shown in Figure 3-1 while the second used the same geometry with the AICA walls disabled. The AICAs average 17.57 mm in length and have an average diameter of 0.81 mm and area of 0.515 mm^2 at the outlets. These models are referred to as the "no-AICA" model and the "with-AICA" model both here and in the results section. Transient data file "postoperative" was used for both simulations.

Initial studies were performed on both versions with pressure values of 0 Pa assigned at all pressure outlets. Next, a simulation was performed with a constant pressure of an arbitrary value applied to the AICA outlets. A series of simulations were performed using the same model where a different constant pressure was applied at the AICA outlets to iteratively

determine a value which would create a similar mass flow distribution as was obtained in the "with-AICA" model. All other pressure outlets were kept at a value of 0 Pa for these studies.

3.5.1.2. AICA Length: Patient 2 Sump Model

This study continues the investigation from the previous study by comparing three versions of the Patient 2 "sump" geometry. The first version used the model shown in Figure 3-4. The second version used the same model with the AICA wall features disabled. A third version of the model has AICAs of an intermediate length. These models will be referred to as the "no-AICA", "short-AICA" and "long-AICA" model here and in the results section.

The AICAs in the "long-AICA", standard model are an average of 17.47 mm in length and have an average diameter of 0.80 mm and area of 0.504 mm^2 at the outlets. The AICAs in the "short-AICA" model average 5.93 mm in length and have an average diameter of 0.80 mm and area of 0.501 mm^2 at the outlets. Transient data file "AICA sump 2" was used for all three versions of the model.

The same iterative method described in the previous study was used to determine pressure values at the AICAs in the "no-AICA" model to emulate both the "short-AICA" and "long-AICA" versions. Additionally, the "short-AICA" model is compared to the "long-AICA" model in the same fashion.

3.5.1.3. Perforator Quantity

This study investigates the impact on flow patterns using differing quantities of perforators using the Patient 2 "preop" geometry. The base model shown in Figure 3-3 has 13 total perforators. Four studies were performed; one with all 13 perforators present, one with no perforators, one with 6 perforators and one with 8 perforators. Perforators were removed

in a pattern intended to leave the remaining perforators as evenly distributed across the basilar trunk as possible. Transient data file "preoperative" was used for all four versions of the model.

3.5.1.4. Lateral Branch Diameter

This study investigates the impact of perforator and AICA diameters by comparing two versions of the Patient 2 "preop" geometry. The first simulation used the version shown in Figure 3-3. For the second version, both the AICAs and perforators were increased in diameter by a uniform value.

The model version with the standard geometry has an average AICA length of approximately 17.47 mm. The average AICA diameter is 0.801 mm and the area is 0.504 mm^2 measured at the outlets. There are 13 total perforators with an average length of 7.43 mm with a standard deviation of 1.113 mm. The average perforator diameter is 0.329 mm, with a 0.085 mm^2 area at the outlets.

The model with the enlarged lateral branches has an average AICA length of 17.46 mm The average AICA diameter is 1.01 mm and the area is 0.797 mm^2 measured at the outlets. There are 13 total perforators with an average length of 7.42 mm with a standard deviation of 1.028 mm. The average perforator diameter is 0.531 mm, with a 0.221 mm^2 area at the outlets. Transient data file "preoperative" was used for both versions of the model.

Due to the non-uniform nature of the geometry, the process of increasing the outlet diameters caused discontinuities in the model. As a result, several of the perforators were relocated or shortened during the creation of the "large outlet" version of the geometry.

3.5.1.5. Perforator Location

This study investigates any changes in flow due to variations in perforator location by comparing two versions of the Patient 2 "preop" model. The first version used the model shown in Figure 3-3. For the second version, the perforators were relocated approximately 45° around the center of the basilar towards the anterior. Figure 3-9 shows a sketch of the intent of the perforator relocation.

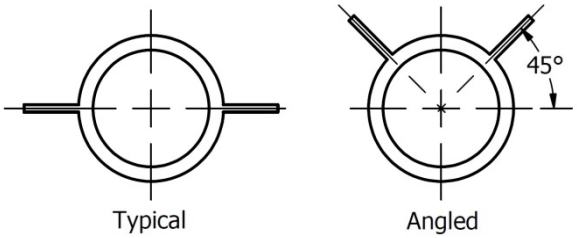

Figure 3-9: Location Study: Perforator Orientation

Due to the non-uniform nature of the basilar trunk surface, this angle was estimated visually for each perforator. In some cases, perforators required further rotation, lengthening or shortening to resolve discontinuities. They were oriented so that their walls were approximately normal to the surface of the basilar artery at their junction to eliminate surface angle as a variable. Transient data file "preoperative" was used for both versions of the model.

3.5.2. Apex Pressure Studies

When modifying the model, it is more difficult to confidently extend the length of the apex arteries, as it requires the inclusion of the distal bifurcations and branches, as opposed to the side branches which are already being created by the user. Rather than adding length to these outlets, length can be simulated using a constant distal pressure value, as described in the AICA length studies.

The studies described in this section investigate the effect on flow patterns caused by using applying a constant distal pressure at the apex of the outlets. The pressure values are adjusted iteratively using the method described in Section 3.5.1 to reach a predetermined flow distribution target.

3.5.2.1. Apex Pressure: Single Patient Comparison

In this study, the target performance is a 90%/10% ratio of mass flow rates between the apex and lateral branches respectively. The simulations were performed on the Patient 2 "preop" model shown in Figure 3-3, using the transient data file "preoperative".

For the second part of the study, the same pressure value determined on the "preop" model was applied to the apex outlets of the Patient 2 "sump" model shown in Figure 3-4, using the "AICA Sump 2" transient data file. The right PCA is the primary inlet for this geometry, so the elevated pressure value was applied to the other three apex outlets only. All other pressure outlets in these simulations were left at a value of 0 Pa.

3.5.2.2. Apex Pressure: Differing Physiology

In this study, the apex pressure value determined for the Patient 2 "preop" model is applied to the apex outlets of the two versions of the Patient 1 model. For the first of these studies, the model used was the Patient 1 "sump" model shown in Figure 3-2. The transient data file used was the "AICA sump 1" file. As the right PCA is the primary inlet for this geometry, the pressure value was applied to the other three apex outlets.

The second study was performed on the Patient 1 "bypass" model shown in Figure 3-1. The transient data file used was the "reimplanted SCA" file. Three of the four apex outlets are used as part of a bypass system, so the pressure value was applied only to the right SCA.

3.5.2.3. Tracer Study

A second approach to analyze blood flow behavior is to determine the flow residence time by examining filling and washout patterns. This is accomplished by introducing a tracer agent at the inlets and observing its progression over five cardiac cycles. If the AICAs and perforators are not filled at the end of the simulation, they are likely to become thrombosed.

The simulations used the Patient 1 "sump" geometry, shown in Figure 3-2, and the transient data file "AICA sump 1". The simulations were performed for a total of 164 time steps, which equates to 4.075 seconds, or approximately 5.13 total cardiac cycles.

3.5.3. Mesh Data

Figure 3-10 is a reference table listing the element type and element quantity for each of the simulations.

Study	Base Model	Element Type	Element Quantity
Length1: Long AICA	Patient 1 Bypass	Tetrahedral	1,369,224
Length1: No AICA	Patient 1 Bypass	Tetrahedral	1,328,980
Length 2: Long AICA	Patient 2 Sump	Tetrahedral	812,757
Length 2: Short AICA	Patient 2 Sump	Tetrahedral	803,712
Length 2: No AICA	Patient 2 Sump	Tetrahedral	790,396
Quantity: 13	Patient 2 Preop	Tetrahedral	961,605
Quantity: 8	Patient 2 Preop	Tetrahedral	922,078
Quantity: 6	Patient 2 Preop	Tetrahedral	904,065
Quantity: 0	Patient 2 Preop	Tetrahedral	857,062
Diameter: Regular	Patient 2 Preop	Tetrahedral	961,605
Diameter: Large	Patient 2 Preop	Tetra/Prism Mix	1,843,024
Location: Standard	Patient 2 Preop	Tetrahedral	961,605
Location: Moved	Patient 2 Preop	Tetrahedral	702,852
Apex Pressure 1	Patient 2 Preop	Tetrahedral	961,605
Apex Pressure 2	Patient 2 Sump	Tetrahedral	812,757
Apex Pressure 3	Patient 1 Sump	Tetrahedral	1,224,168
Apex Pressure 4	Patient 1 Bypass	Tetrahedral	1,371,225
Tracer Study	Patient 1 Sump	Tetrahedral	1,371,225

Figure 3-10: Mesh Element Quantity

3.6. **Summary**

They primary purpose of this chapter is to describe the studies which were performed and analyzed in the following chapters. However, a description of a study is not sufficient without the foundational information upon which the study is built. All variables must be defined, and all decisions made while performing the simulations must be described. The information presented in this chapter gives this foundation, allowing the results to be easily repeated, modified or refuted.

The studies investigate a broad range of geometry changes, but with a small number of versions compared with each change. The results will give a general idea of the patterns and tendencies caused by these differences but will lack the more thorough, in-depth analysis required to create a predictive algorithm. The thesis can act as either a rough guideline for the creation of lateral basilar branches in clinical research or as an initial step for more focused research.

4. Simulations

4.1. Chapter Overview: Data Presentation

In this chapter, the results of the simulations are presented and briefly discussed. A thorough review of the data and discussion of its significance can be found in Chapter 5.

Mass flow data is collected using output monitors applied to the pressure outlets of the models in ANSYS. The data is imported into Excel for calculations and table creation. The mass flow results at each outlet are taken as an average across all time steps. Each apex artery and AICA are each kept as separate data sets while the flow results from the perforators are added together as one data set for easier management. The data is generally displayed as a percentage of the overall flow, allowing for easier comparison of flow performance when dissimilar models have different mass flow rates.

Velocity streamlines are used to analyze three-dimensional flow patterns. For model comparison, the streamline velocities are scaled to the same magnitudes within each study. When reviewing streamline results, regions of low flow velocity, or flow recirculation can indicate regions prone to thrombus deposition. This type of flow behavior is typically observed in the aneurysmal part of the artery.

WSS distributions are used to allow for the analysis of flow velocity on a smaller scale than what is shown in the velocity streamlines. The results are similarly scaled for easier comparison of results. Low WSS would indicate a low shear at the arterial wall, which is also a sign of thrombus deposition.

The final method used is a passive tracer fill map. The mesh elements where the tracer concentration exceeds a value of 0.5 are displayed in red. This type of analysis assesses flow

residence time, indicating whether or not fresh blood is being sufficiently supplied throughout the system.

4.2. AICA Length Studies

Two sets of studies were performed to determine the effect of the length of the AICA branches on the flow distribution among the outlets and the flow patterns through the basilar artery. As the vessel walls are assumed to be rigid, a constant distal pressure may be used as a replacement for the friction losses of longer outlets.

4.2.1. Length Study 1: Long AICAs vs. No AICAs

This study uses the Patient 1 geometry shown in Figure 3-1. The first simulation was performed on the unmodified model as displayed in the figure. The remaining simulations were performed on the same model with the AICAs removed.

The initial simulation was performed with all pressure outlets set to a constant 0 Pa distal pressure. The flow distribution results are shown in the first row of Table 4-1.

Table 4-1: Length Study, Patient 1, Pressure Determination

Model	Pressure at AICAs (Pa)	Outputs			
		SCA Outlet	AICAs	Perfs	Total Branch
w/AICA	0	83.195%	12.962%	3.843%	16.805%
no AICA	0	52.721%	45.764%	1.515%	47.279%
no AICA	500	88.539%	7.895%	3.566%	11.461%
no AICA	425	83.532%	13.260%	3.208%	16.468%
no AICA	420	83.186%	13.629%	3.184%	16.814%

A series of simulations were then performed on the “no-AICA” model. In each version, a constant distal pressure was applied to the AICAs as indicated in the second column of Table 4-1. The results were reviewed, and the pressure value was adjusted until the flow distribution

was close to that of the “with- AICA” model. The pressure at all other outlets was kept at a constant 0 Pa throughout.

Figure 4-1 shows a side-by-side comparison of the two models with 0 Pa distal pressure at all outlets. With no wall length for the AICA outlets and no distal pressure, there is little resistance to flow, creating a sharp increase in velocity in the region of the AICA outlets in the “no-AICA” version. This velocity increase extends into the vertebral arteries. This result corresponds to what is shown in the second row of Table 4-1: where outlet flow at the AICAs represents nearly half of the overall outlet flow.

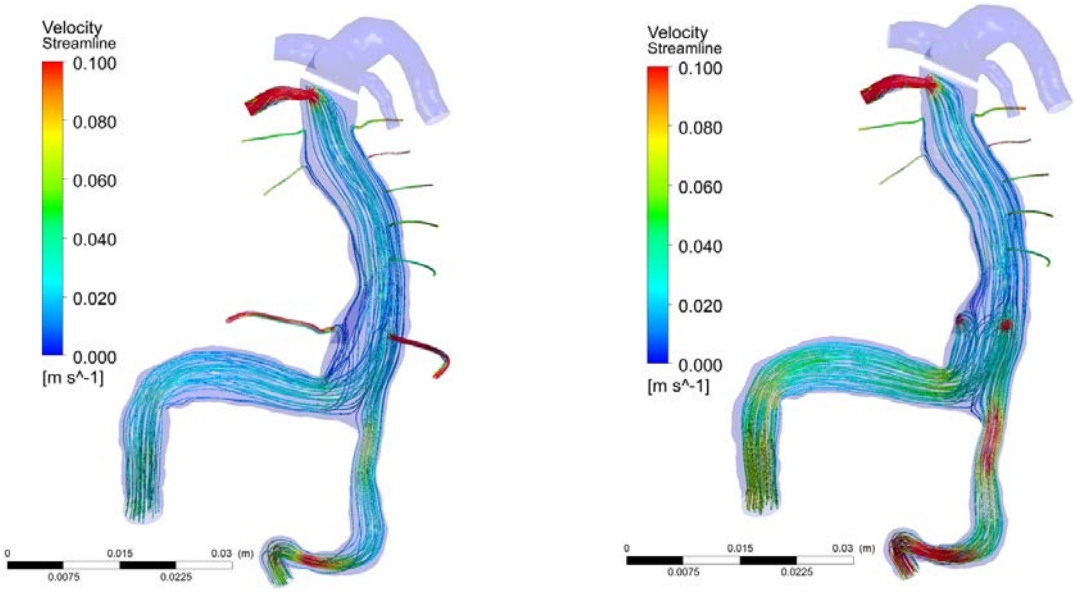

(a) “with-AICA” (b) “no-AICA”

Figure 4-1: Length Study: Patient 1 Bypass, Preliminary Comparison

In Figure 4-2, the same streamline results for the “with-AICA” model are compared with the results from the “no-AICA” model simulation using the final AICA distal pressure value of 420 Pa. In this comparison, the velocity magnitudes appear to be quite similar between the

two models. The flow patterns in the region of the AICA outlets are notably different. A small region near the AICA outlets indicates a change in flow patterns. The flow appears to increase in velocity and align with the AICA outlets, with the result of altering the overall flow patterns in the lower region of the basilar artery.

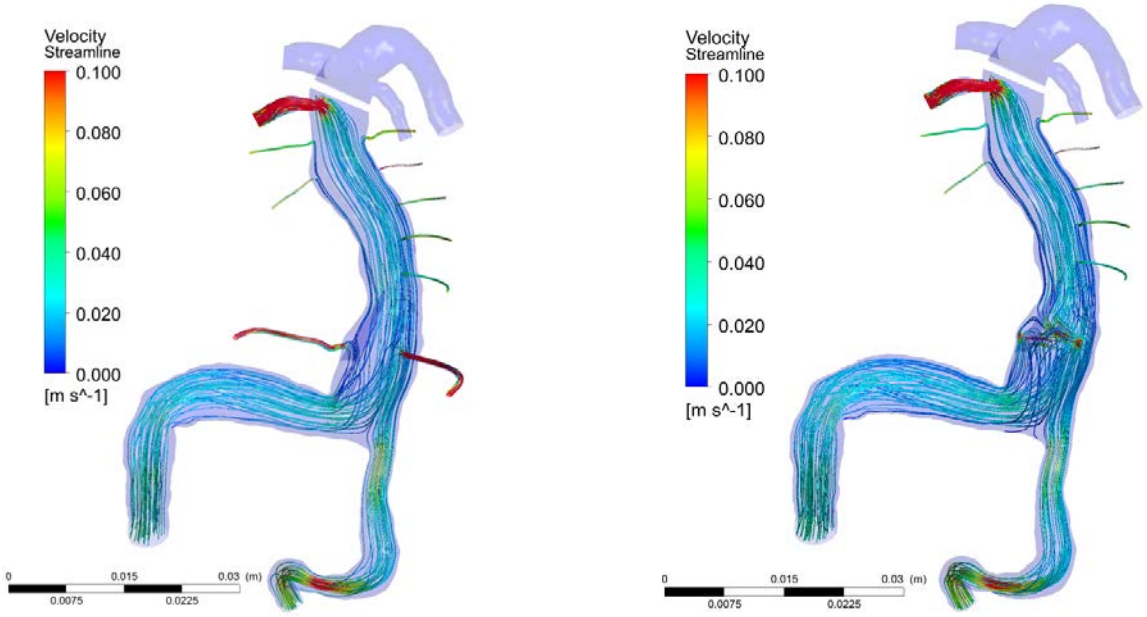

(a) "with-AICA", 0 Pa at all outlets

(b) "no-AICA", 420 Pa at AICAs

Figure 4-2: Length Study: Patient 1 Bypass, AICA Pressure Comparison

4.2.2. Length Study 2: Long AICAs vs. Short AICAs

The second AICA length study introduces an intermediate length of the AICAs which allows for a greater number of comparisons between model versions.

The same iterative procedure established in Length Study 1 was used to determine pressure values at the AICA outlets. In this case, pressure values were determined which would be applied to the "no-AICA" version which would replace both the long and short version. The third set of simulations determined the pressure to be applied to the AICAs of the

"short-AICA" model to replace the extra length present in the "long-AICA" version. The results of these investigations are shown in Table 4-2.

Table 4-2: Length Study: Patient 2, Pressure Required for Length Equivalency

Simulated Model	Target Model	Simulated Model AICA Length (mm)	Target Model AICA Length (mm)	Length Difference (mm)	Applied Pressure (Pa)	Pressure per Length (Pa/mm)
No AICAs	Short AICAs	0.00	5.93	5.93	21.76	3.67
No AICAs	Long AICAs	0.00	17.47	17.47	24.40	1.40
Short AICAs	Long AICAs	5.93	17.47	11.54	19.30	1.67

Reviewing the pressure values in the "no-AICA" comparisons, the relationship between AICA length and the distal pressure required to replace them appears to be nonlinear. It is hard to determine an exact trend with only three data points.

There is also an unusual relationship in the required distal pressures. The distal pressure value applied to the "no-AICA" model to emulate the "short-AICA" version is 21.76 Pa and the value used to emulate the "long-AICA" version is 24.40 Pa, which gives a difference of 2.64 Pa between the two model versions. However, the pressure value applied to the "short-AICA" model to emulate the "long-AICA" model is much higher, at 19.3 Pa.

The previous study showed that, with no distal pressure applied, the "no-AICA" model version exhibited increased velocity and altered flow patterns near the AICA outlets. Figure 4-3 is shown here to look for similar patterns in the Patient 2 model. The velocity scale of the two simulations is different between the models, but the flow patterns bear strong similarities. Both have a redirection of flow streamlines and a sharp increase in velocity near the AICA outlets.

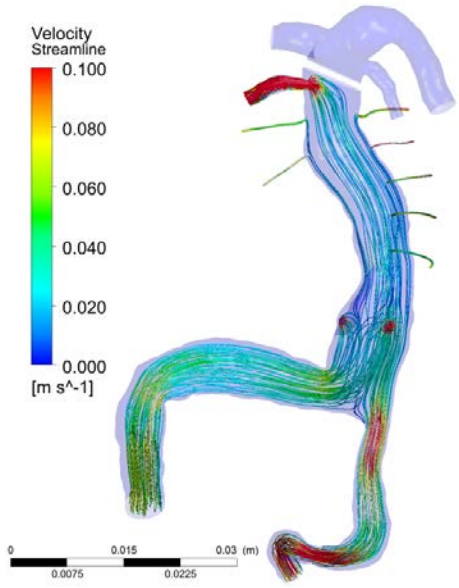

(a) Patient 1, "no-AICA", 0 Pa at All Outlets

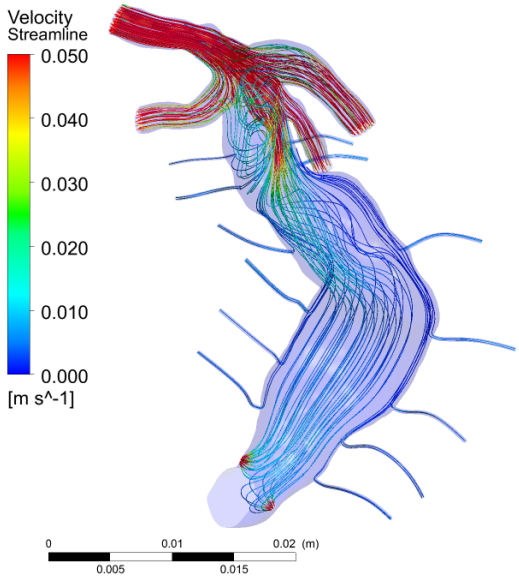

(b) Patient 2, "no-AICA", 0 Pa at All Outlets

Figure 4-4: Length Study: Streamline Comparison between the "no-AICA" Models

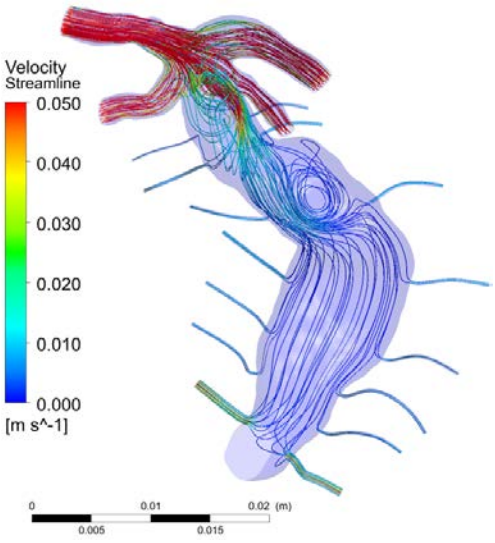

(a) "short-AICA", 0 Pa at All Outlets

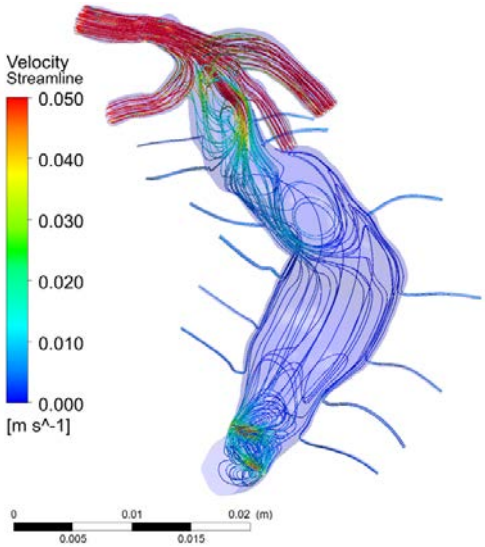

(b) "no-AICA", 21.76 Pa at AICAs

Figure 4-3: Patient 2, "short-AICA" vs. "no-AICA" with 21.76 Pa

In Figure 4-4, the "short-AICA and "no-AICA" versions of the model are compared, with the equivalent distal pressure of 21.76 Pa applied to the AICA outlets of the no-AICA model.

The velocity magnitudes are similar, but the “no-AICA” model has the region of increased velocity within the basilar and corresponding flow pattern change as was seen in Figure 4-2. There is a region of recirculation near the apex of both models which appears to be larger in diameter in the “no-AICA” model. The small magnitude of the difference indicates that this change is possibly due to streamline scaling parameters, but it is worth noting for comparison to similar patterns present in later studies.

Figure 4-5 shows the comparison between the “long-AICA” model with 0 Pa distal pressures and the “no-AICA” model with a 24.4 Pa distal pressure applied to each of the AICAs. The same flow pattern and velocity change near the AICAs are present in this comparison. Additionally, the flow patterns near the apex are altered as they were in Figure 4-4, but to a larger degree. The flow seems to travel in a straighter path through the region with the aneurysm in the “no-AICA”.

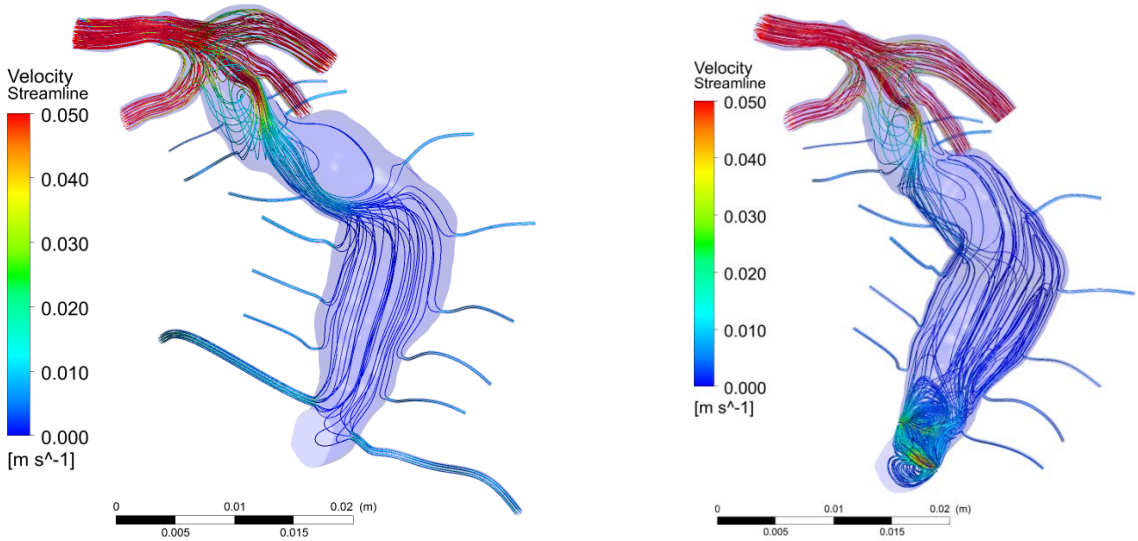

(a) “long-AICA”, 0 Pa at All Outlets

(b) “no-AICA” 24.4 Pa at AICAs

Figure 4-5: “long-AICA” vs. “no-AICA” with 24.4 Pa Pressure

Figure 4-6 shows the final comparison; the "long-AICA" version with 0 Pa outlet pressures compared to the "short-AICA" version with a 19.3 Pa distal pressure at the AICAs. The overall flow patterns between these two versions are very similar, which indicates that the presence of some length of outlet wall is necessary to eliminate the formation of the high-velocity region near the AICAs.

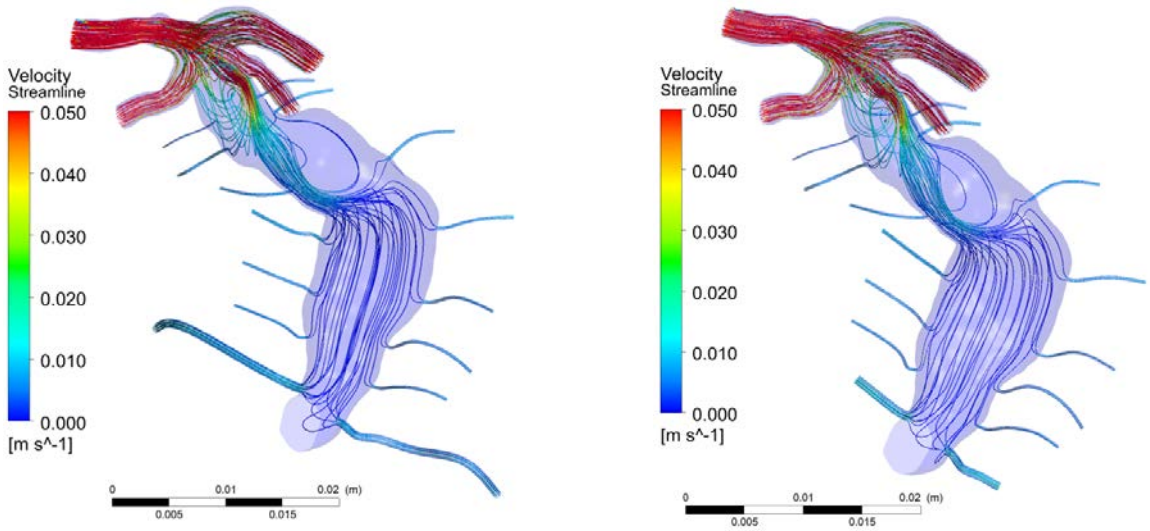

(a) "long-AICA", 0 Pa at All Outlets

(b) "short-AICA", 19.3 Pa at AICAs

Figure 4-6: Patient 2, "long-AICA" 0 Pa vs. "short-AICA", 19.3 Pa Pressure

4.3. Perforator Quantity Study

A series of four simulations were performed for this study, each using a version of the Patient 2 geometry with a different quantity of perforator outlets. The results of these simulations are shown in Table 4-3. The table compares the overall increase in flow through the apex outlets against that of the lateral branches.

Figure 4-7 shows the relationship between the number of outlets and amount of flow to be approximately linear. The fit line is linear with an R^2 value of 0.9996. More data points would be required for a deeper analysis of this result. As the number of perforators in

increased, the total cross-sectional area of the perforator outlets increases, and the percentage of total outlet flow through the perforators increases nearly linearly. At the same time, the overall area of the outlets for the entire basilar artery also increases, reducing the average velocity at each outlet which accounts for the R^2 deviating from a value of 1.

The velocity streamline results of the four different versions of the model are shown in

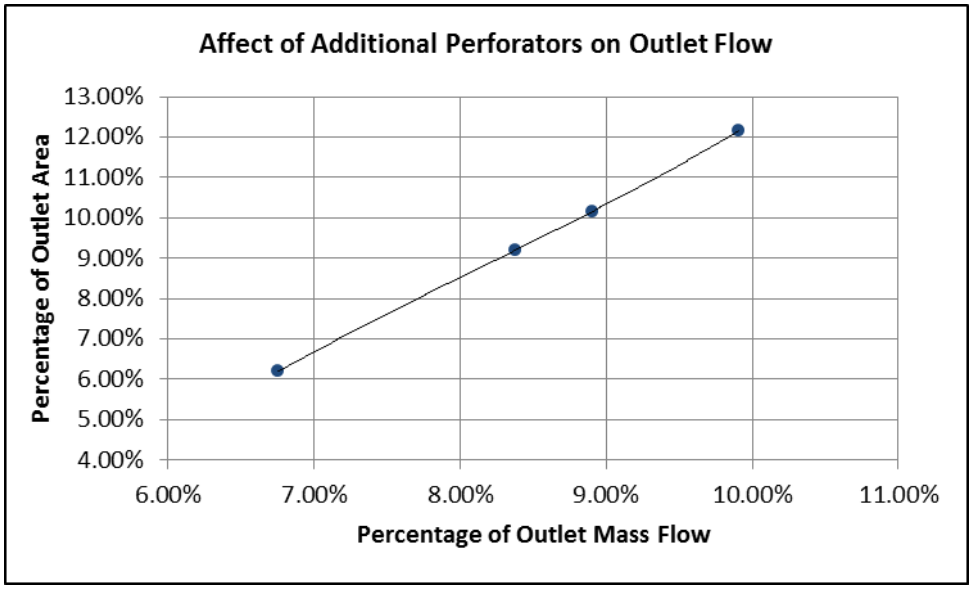

Figure 4-7: Perforator Area to Flow Comparison

Table 4-3: Perforator Quantity Flow Distribution Comparison

# Perfs	% of Outlet Flow		Outlet Area (mm^2)		% of Outlet Area	
	Apex Arteries	Lateral Branches	Apex Arteries	Lateral Branches	Apex Arteries	Lateral Branches
0	93.25%	6.75%	15.273	1.008	93.81%	6.19%
6	91.62%	8.38%	15.273	1.547	90.80%	9.20%
8	91.09%	8.91%	15.273	1.728	89.84%	10.16%
13	90.09%	9.91%	15.273	2.112	87.85%	12.15%

Figure 4-8. There are no notable changes in the flow patterns between these versions, but there is a decrease in velocity within the AICAs and perforators as the number of perforators increases.

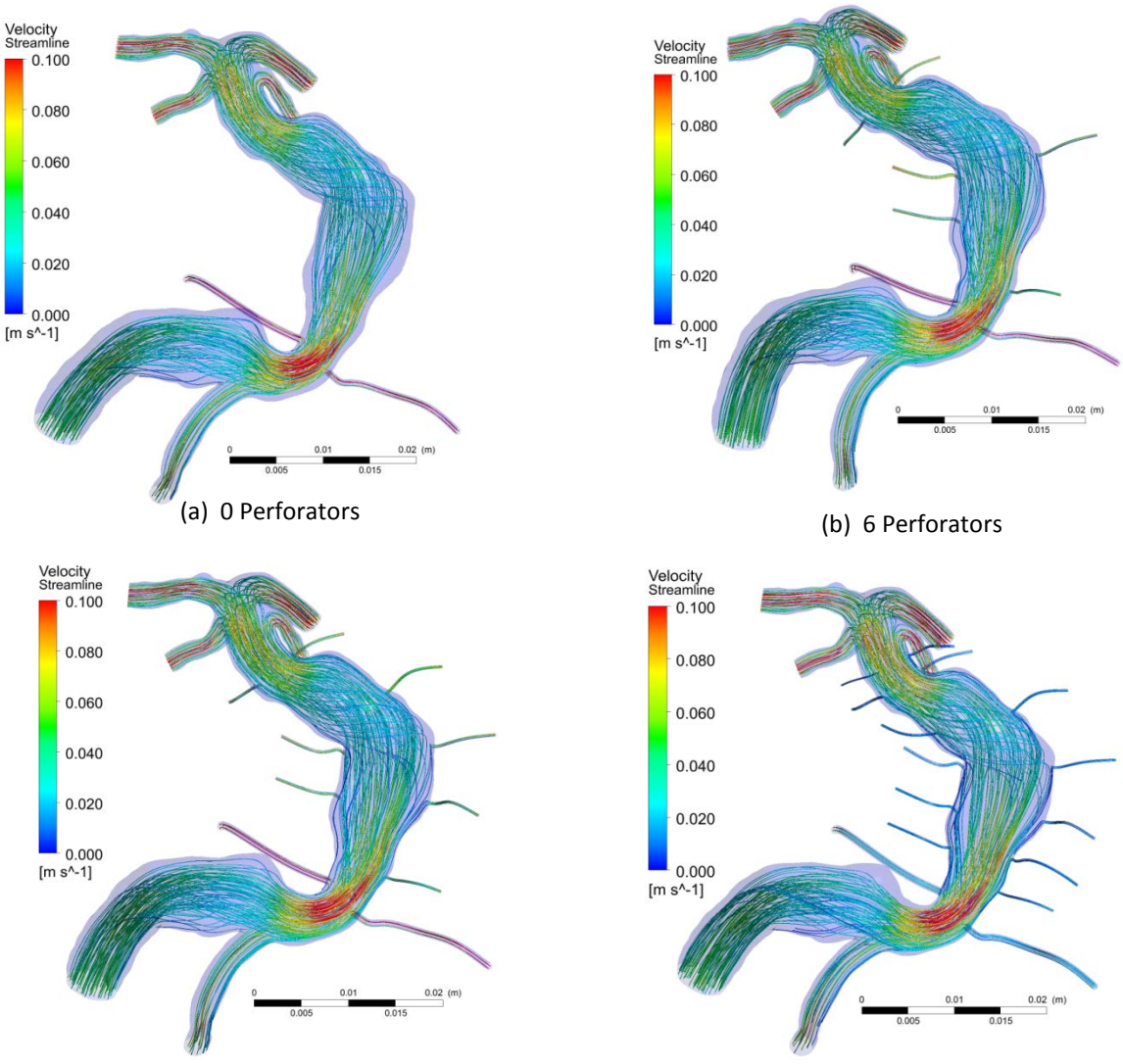

(a) 0 Perforators

(b) 6 Perforators

(c) 8 Perforators

(d) 13 Perforators

Figure 4-8: Perforator Quantity, Streamline Comparison

4.4. **Lateral Branch Diameter Study**

For this study, two versions of the patient 2 "preop" geometry were simulated and compared. One with the outlet diameters established in the base model and the second with both the perforators and the AICAs increased in diameter by the same value.

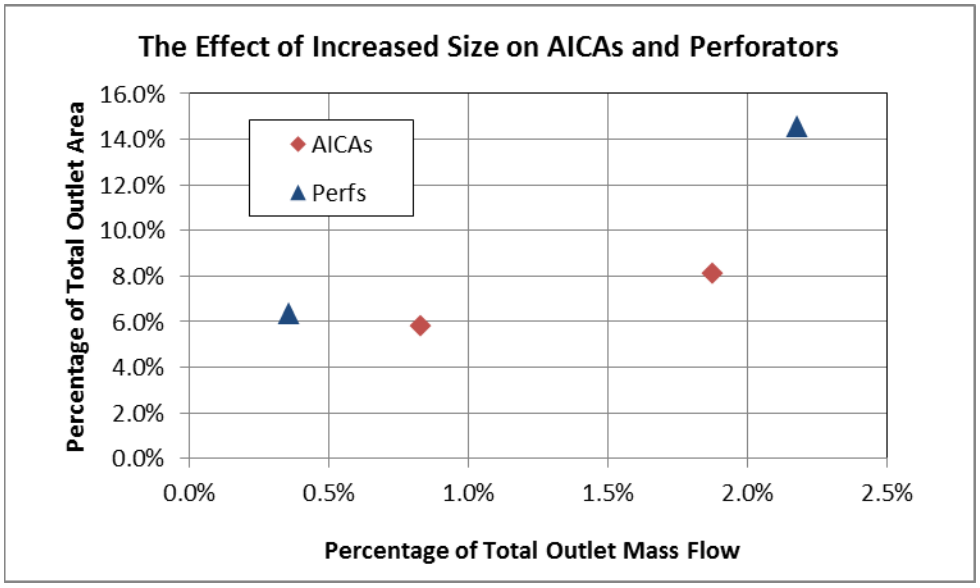

Figure 4-9: Diameter Study: Outlet Flow Change Comparison

This change causes a greater relative increase in area for the smaller perforators than for the AICAs, which would lead to a relatively greater increase in blood flow through the perforators. The results shown in Figure 4-9 reflect this trend, but the comparison looks at outlet area which should compensate for the difference, indicating a similar increase in both outlet types per area increase. The results do not show a linear relationship, as the perforators have an even greater increase in flow than would be expected using that assumption.

The relationship will instead follow Poiseuille's law for laminar flow through a small tube, which relates flow resistance to the fourth power of the tube radius. Table 4-5 compares

Table 4-4: Diameter Study: r^4 and Mass Flow Comparison

	Avg Radius (mm)		Radius^4 (mm^4)		Average Flow per Outlet (mg/s)	
	AICAs	**Perforators**	**AICAs**	**Perforators**	**AICAs**	**Perforators**
Regular	0.0158	0.0064	6.16E-08	1.73E-09	7.0461	0.4684
Large	0.0198	0.0104	1.54E-07	1.18E-08	15.9615	2.8540
Increase	0.0041	0.0040	9.26E-08	1.01E-08	8.9154	2.3856
% increase	25.78%	61.85%	150.32%	586.17%	126.53%	509.29%

the outlet flow values using this relationship. A more detailed discussion of this relationship can be found in the following chapter.

For a better analysis of the effect of the velocity changes due to the increased diameters, WSS comparisons between the two versions were performed on the left AICA and one of the perforators. These comparisons are shown in Figure 4-10 and Figure 4-11 respectively.

As a final part of the analysis, Figure 4-12 shows a comparison of the streamlines of the two model versions. The only notable difference is a decreased velocity in the perforators in the version where the perforators are enlarged. The flow patterns themselves appear to be unaffected by the increased outlet size.

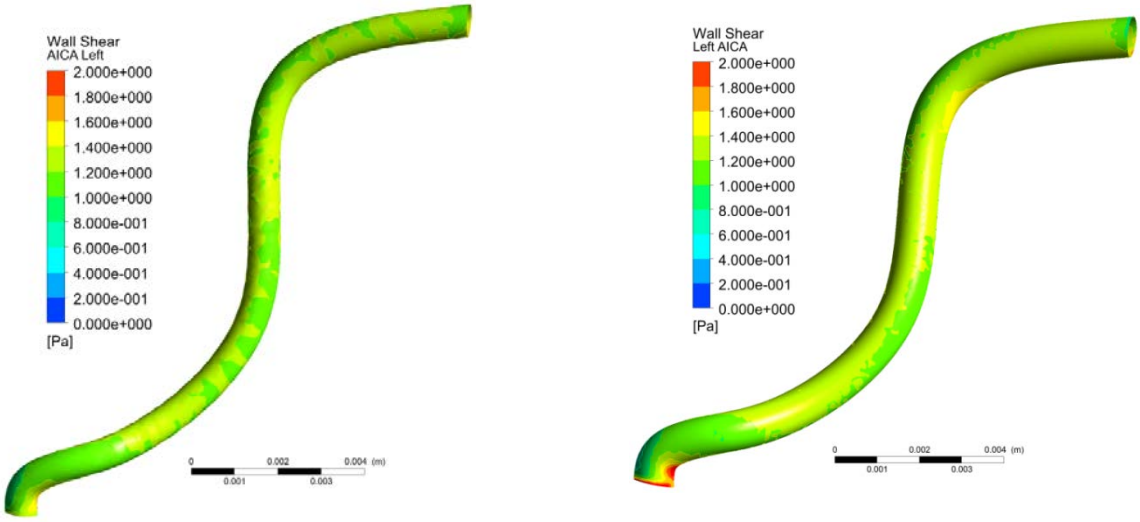

(a) Small Outlets (b) Large Outlets

Figure 4-10: Diameter Study: Left AICA WSS Comparison

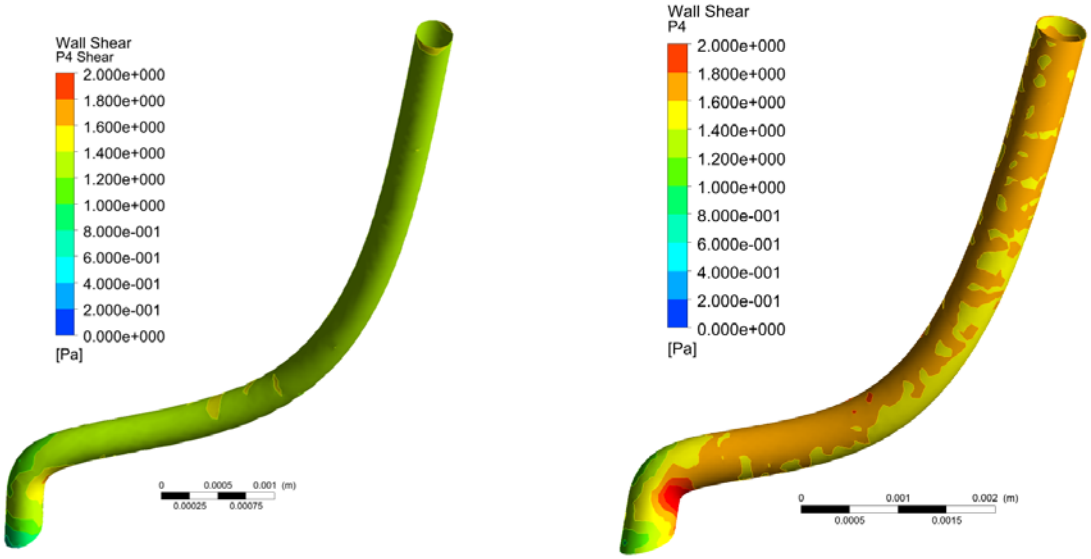

(a) Small Outlets (b) Large Outlets

Figure 4-11: Diameter Study: Perforator WSS Comparison

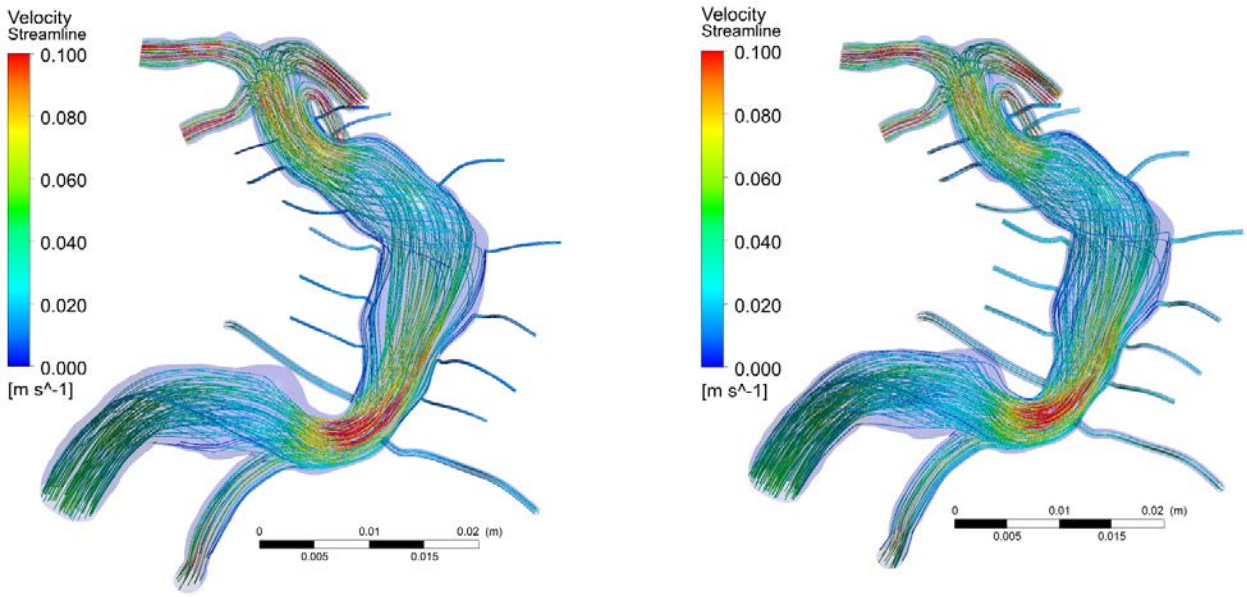

(a) Small outlets

(b) Large Outlets

Figure 4-12: Diameter Study: Streamline Comparison

4.5. Perforator Location Study

For this study, the perforators were relocated towards the posterior of the basilar artery while keeping size and quantity constant. The distribution results are shown in Table 4-6. These results show a slight increase in flow to both categories of lateral branches as well as the SCAs, with the PCAs being the only outlet with a reduction. The changes to the flow distribution are too small to form any conclusions with certainty.

Table 4-5: Location Study: Outlet Flow Distribution

Orientation	% of Total Outlet Flow				Total Apex	Total Branches
	SCAs	PCAs	AICAs	Perfs		
Regular	27.628%	71.19%	0.828%	0.358%	98.814%	1.186%
45 degrees	27.936%	70.87%	0.838%	0.361%	98.801%	1.199%

The comparison of flow streamlines, shown in Figure 4-13, does not indicate any changes in the flow patterns due to the new perforator locations. Any changes in flow behavior are too small to affect the large-scale flow patterns visible in this type of analysis.

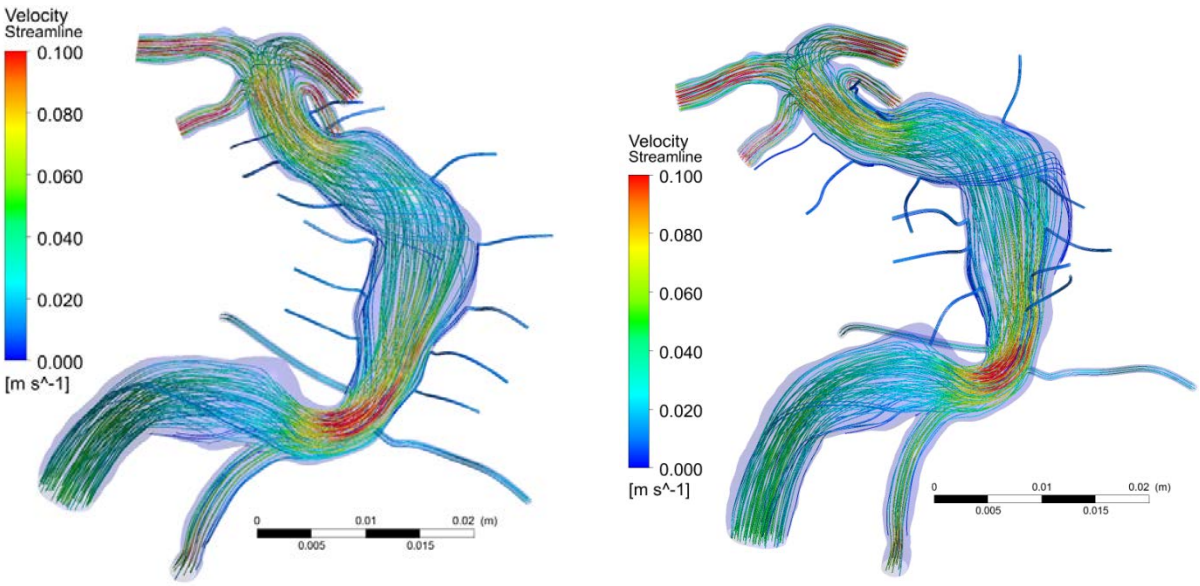

(a) Base Model (b) Relocated Perforators

Figure 4-14: Location Study: Streamline Comparison

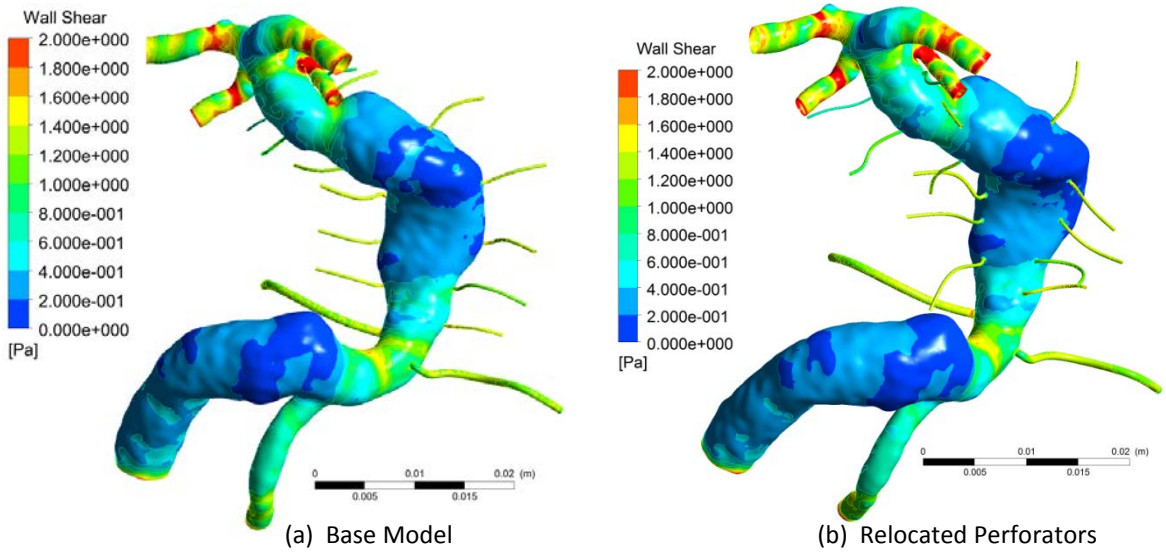

(a) Base Model (b) Relocated Perforators

Figure 4-13: Location Study: Full Model WSS Comparison

A WSS can show subtle changes in flow patterns which may not be apparent in a velocity streamline comparison. The comparison in Figure 4-14 shows that several locations of higher WSS have shifted slightly around the basilar trunk, but they seems to remain localized; directly tied to the location where the perforators join the basilar trunk. Any difference in the overall WSS between the two versions is minimal.

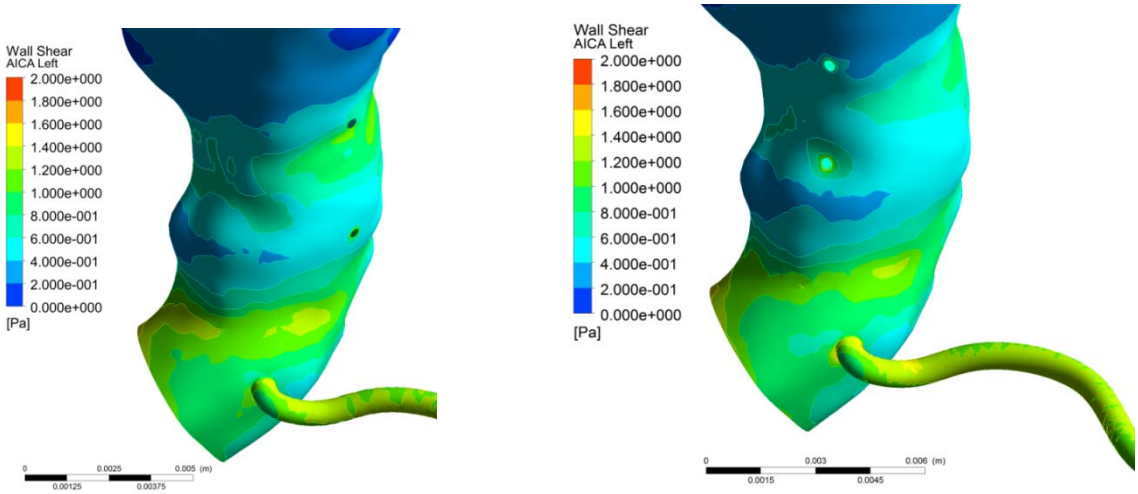

(a) Base Model

(b) Relocated Perforators

Figure 4-15: Location Study: Left AICA WSS Comparison

Figure 4-15 shows the region where the left AICA enters the basilar arterial wall. The perforators are hidden in these images to allow for an unrestricted view of the surfaces.

Localized zones of slightly higher WSS have moved along with the perforators, but the magnitude of the WSS around the perforator connection points is similar between the two versions. There appears to be slightly higher WSS near the base of the AICA after the perforators are relocated. The decreased velocity corresponds with the unmoved perforators, where the perforators are closer to being in-line with the AICAs.

Figure 4-16 is a comparison of the WSS at the base of one of the perforators, including the adjacent region of the basilar wall. The magnitude of the WSS in both the perforator and in

the adjacent basilar wall is unchanged between the two model versions. The WSS patterns have simply relocated with the relocation of the perforator.

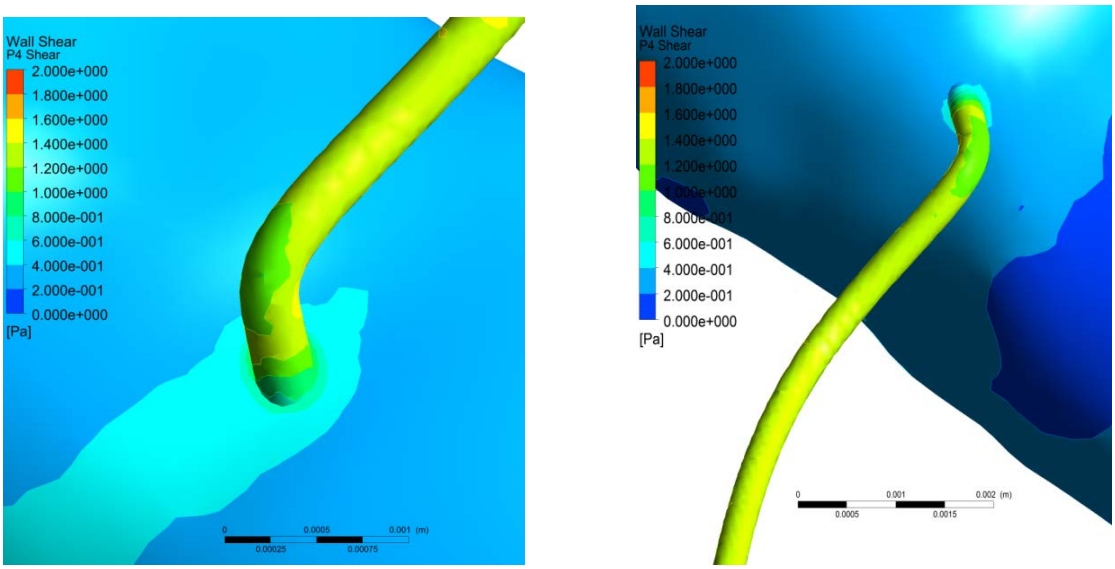

(a) Base Model

(b) Moved Perforators

Figure 4-16: Location Study: Perforator WSS Comparison

4.6. Apex Pressure Studies

4.6.1. Patient 2 Comparison

The first set of studies compares the preoperative and postoperative versions of the patient 2 geometry. The first step is to determine the required distal pressure to reach a 90%/10% ratio of mass flow between the apex and lateral outlets. The same general procedure used in the AICA length studies (Sections 4.2.1 and 4.2.2) is followed to reach the desired result.

Table 4-6: Apex Pressure: Patient 2 Flow Distribution at 319.3 Pa

Model	% of Outlet Flow					
	PCAs	SCAs	AICAs	Perfs	Total Apex	Total Branch
Preop	64.943%	25.06%	6.784%	3.215%	90.000%	10.000%
Sump	36.510%	52.26%	7.614%	3.619%	88.766%	11.234%

The primary difference being that the increased pressure is applied to the SCAs and PCAs leaving the outlet pressure at the AICAs and perforators at 0 Pa. A final pressure value of 319.3 Pa was determined through this process.

In the next simulation, the pressure value of 319.3 Pa is applied to the apex outlets of the post-operative model. This model has an altered flow pattern, with the right PCA being converted into the inlet. This modification will reduce the overall outlet area of the apex outlets and the remaining apex outlets will be closer to the new inlet. Table 4-8 shows a comparison of the flow distribution between the two versions. The significant results are the total apex and branch columns. This comparison shows that the sump model has an increase in the percentage of overall flow through the lateral branches, primarily through the AICAs.

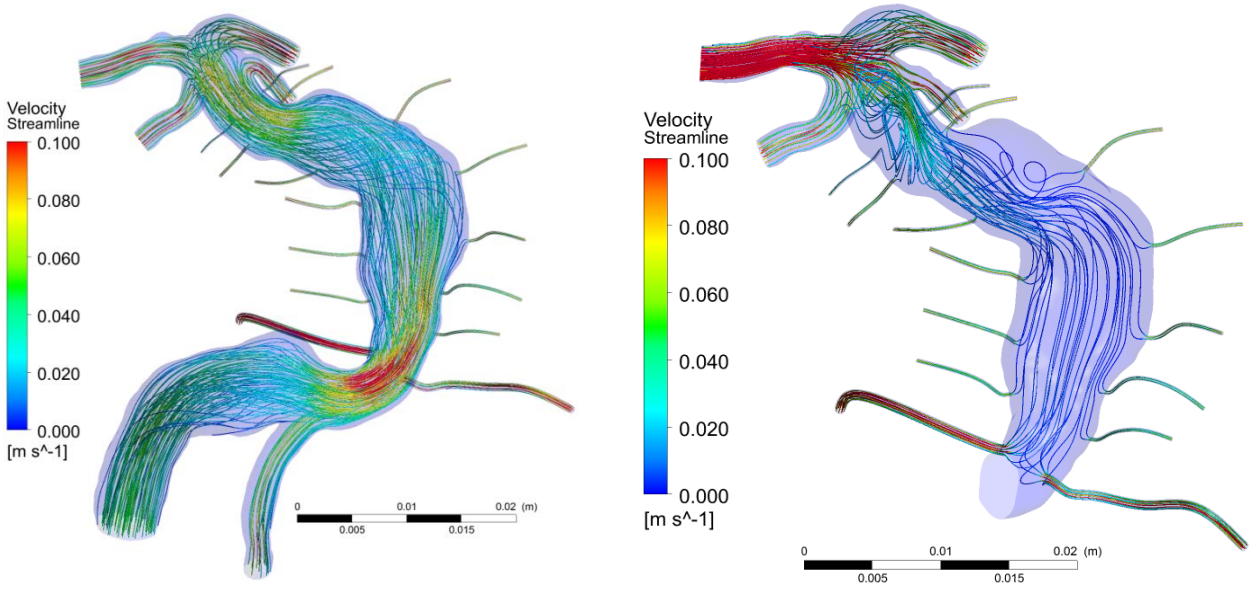

(a) Preop, 319.3 Pa at Apex

(b) Sump, 319.3 Pa at Apex

Figure 4-17: Apex Pressure Study: Patient 2, Preop vs. Sump at 319.3 Pa

For better visualization of flow path changes resulting from the surgery, the velocity streamlines of the two models are compared in Figure 4-17.

The streamlines show similar flow behavior through the lateral outlets between the two versions. The overall flow through the basilar artery itself is reduced, which corresponds with the intent of the sump configuration.

4.6.2. **Apex Pressure: Patient 1 Models**

In this simulation, the same 319.3 Pa distal pressure value is applied to the apex outlets of the Patient 1 "sump" geometry. The difference in time step size, and by extension, the length of cardiac cycle between the two patients is not expected to make a significant difference in the study comparisons. The results are interpreted by viewing the performance over a single cardiac cycle, not over a set period.

A streamline comparison is shown in Figure 4-18, which shows how the flow patterns change with the addition of the distal pressure. The apex pressure version indicates an increase in velocity at the AICAs and perforators, and a general straightening of flow patterns through the basilar artery itself compared to the version with 0 Pa at the apex outlets.

The next simulation is performed on the Patient 1 "bypass" model. Only the right SCA is involved directly in the basilar arterial flow, so it is the only location to receive the 319.3 Pa pressure. As before, all other outlets remain at 0 Pa outlet pressure.

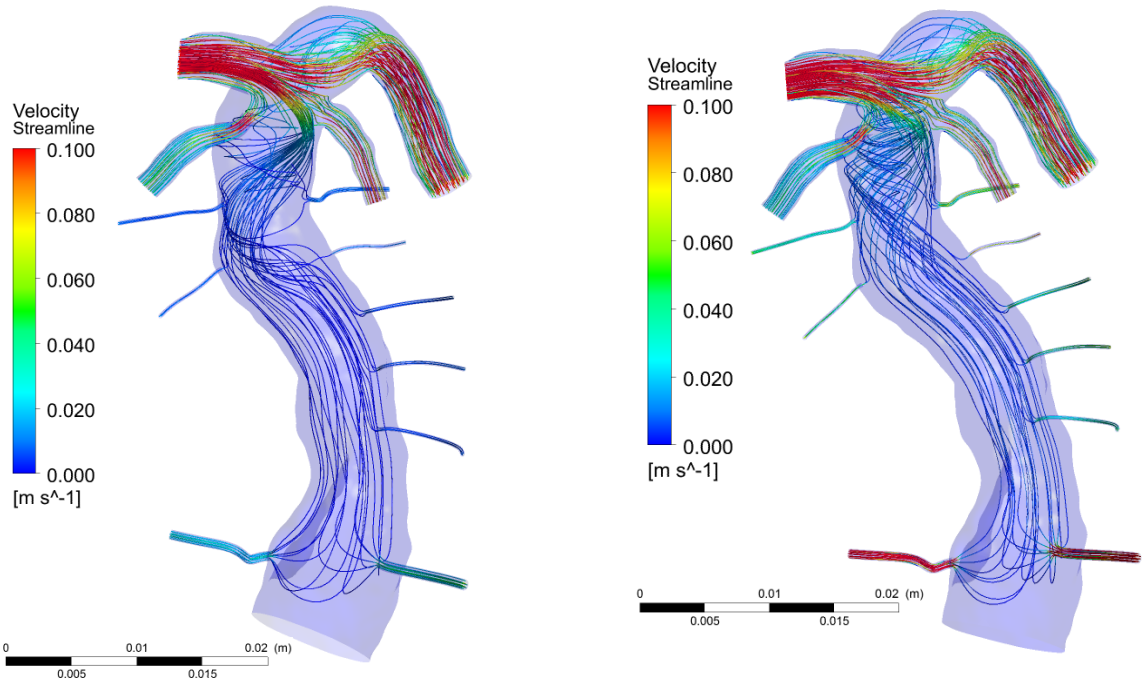

(a) 0 Pa at All Outlets

(b) 319.3 Pa at Apex

Figure 4-19: Apex Pressure: Patient 1 Sump, 0 Pa vs. 319.3 Pa

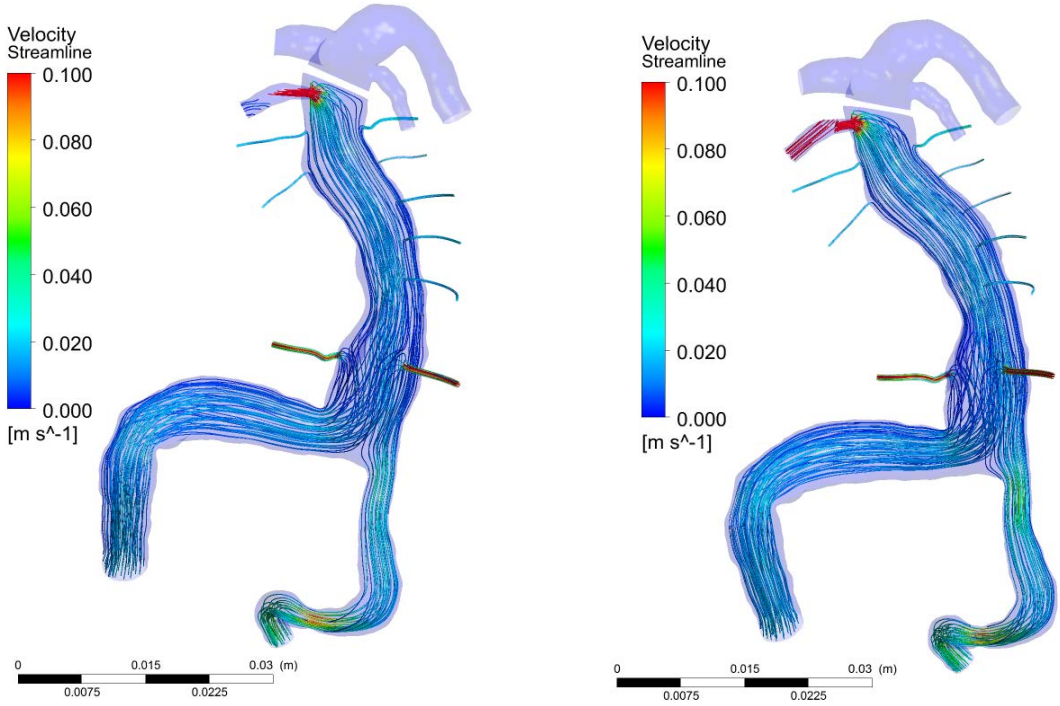

(a) 0 Pa at All Outlets

(b) 319.3 Pa at Apex

Figure 4-18: Apex Pressure Study: Patient 1 Bypass, 0 Pa vs. 319.3 Pa

Figure 4-19 compares the streamlines for the bypass model using 0 Pa apex pressure and the model with the 319.3 Pa applied to the right SCA. There is a higher velocity in the right SCA in the version without 0 Pa, but there are otherwise no major changes in the flow streamline patterns or velocities at the lateral branches.

Figure 4-20 compares the results from all four simulations. The patient 1 sump model has a greater percentage of flow going through the laterals than the patient 2 sump, with a strong bias towards the AICAs. The AICAs on the patient 1 model are shorter, which is likely a contributing factor to this trend.

The patient 1 "bypass" results show a much more significant change in flow distribution. It would seem that adding more pressure to an already restricted outlet has caused more than 90% of the flow to exit the lateral branches. This result does not reflect what would be expected in actual physiology.

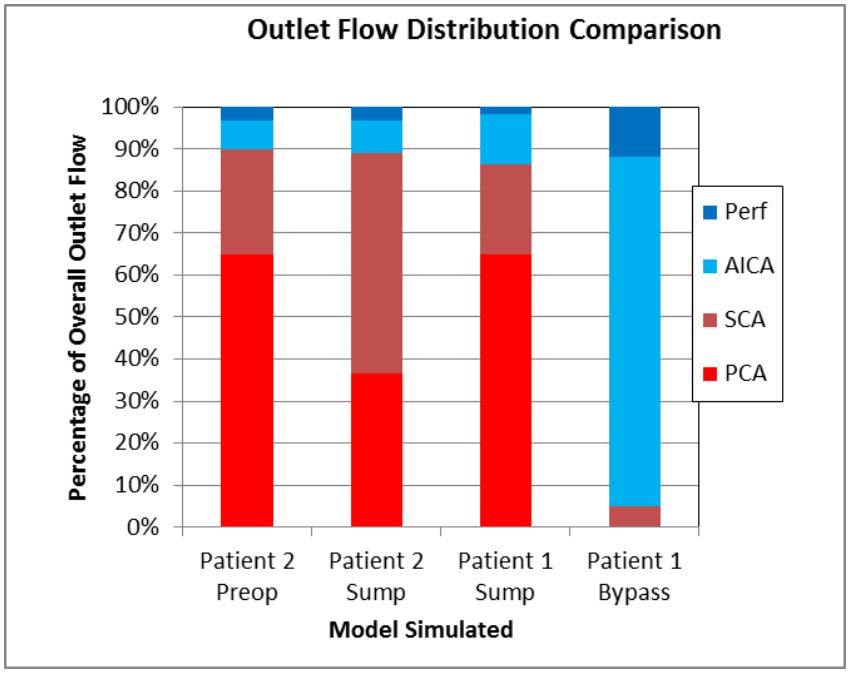

Figure 4-20: Apex Pressure Study: Results Comparison at 319.3 Pa

4.7. **Tracer Study**

The simulations in this study were performed using the Patient 1 “sump” geometry. This study is an extension of the apex pressure studies, so the same distal pressure of 319.3 Pa is applied to the apex outlets as was used in those studies.

These initial results, shown in the middle row of Figure 4-22, indicate insufficient fill of the lateral branches within the simulation. Based on this outcome, additional simulations were performed with the apex pressure adjusted to determine a value where sufficient fill could be achieved. Due to the longer simulation time and the subjective nature of interpreting the results, an “ideal” distal pressure is not determined, but it appears to fall between 1500 and 2000 Pa.

The results from the simulations at three pressure values are displayed in Figure 4-22. The “0 Pa” results are to show a baseline with no additional distal pressure at the apex outlets.

For each pressure value, three time steps were selected as “snapshots”, to give a representation of the fill rate over the cardiac cycles. The first column shows the fill at time step 12, which occurs at 0.275 seconds; less than 1/3 of the first cardiac cycle. These results are reviewed to look for early indications of performance issues in the models.

The second column is at time step 96, which occurs at 2.375 seconds: representing three complete cardiac cycles. The third column shows the results at the end of the simulation: 4.1 seconds.

The final image in the series, Figure 4-22(i), shows that the right AICA begins to fill but the tracer agent has not completely reached the end of the outlet.

There is a certain amount of surging behavior inherent to the pulsatile nature of blood flow. Figure 4-21 shows a closer view of the lower portion of the basilar sump during four times steps near the end of the 1500 Pa simulation, which does not indicate any reduction in the tracer concentration.

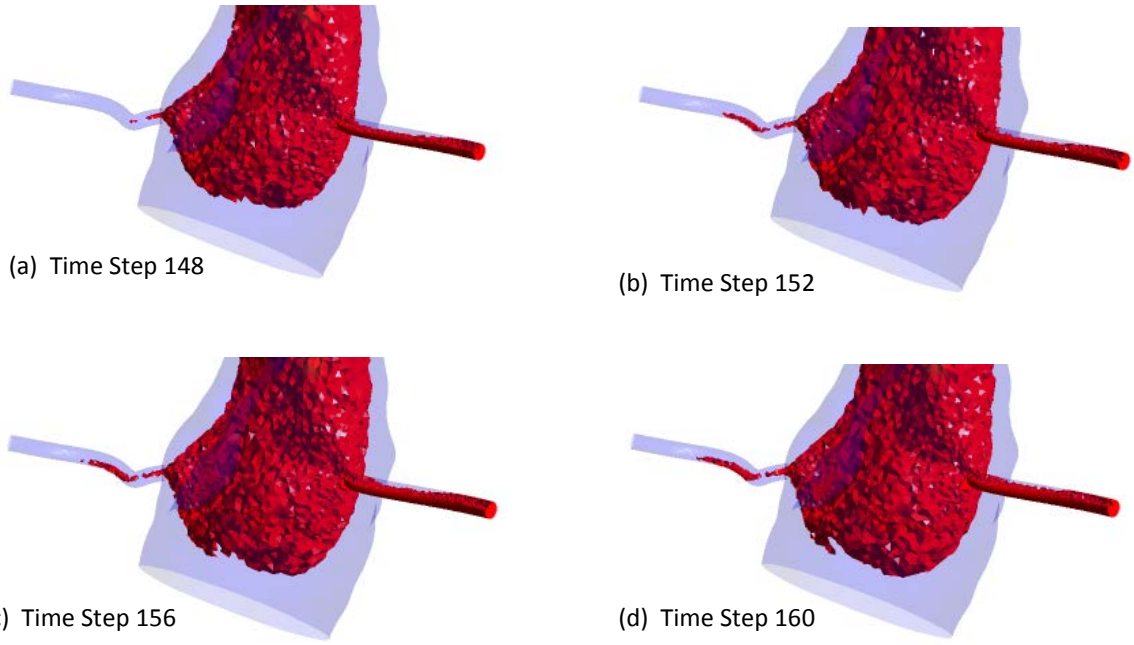

(a) Time Step 148

(b) Time Step 152

(c) Time Step 156

(d) Time Step 160

Figure 4-21: Tracer Study: 1500 Pa Right AICA Fill Rate

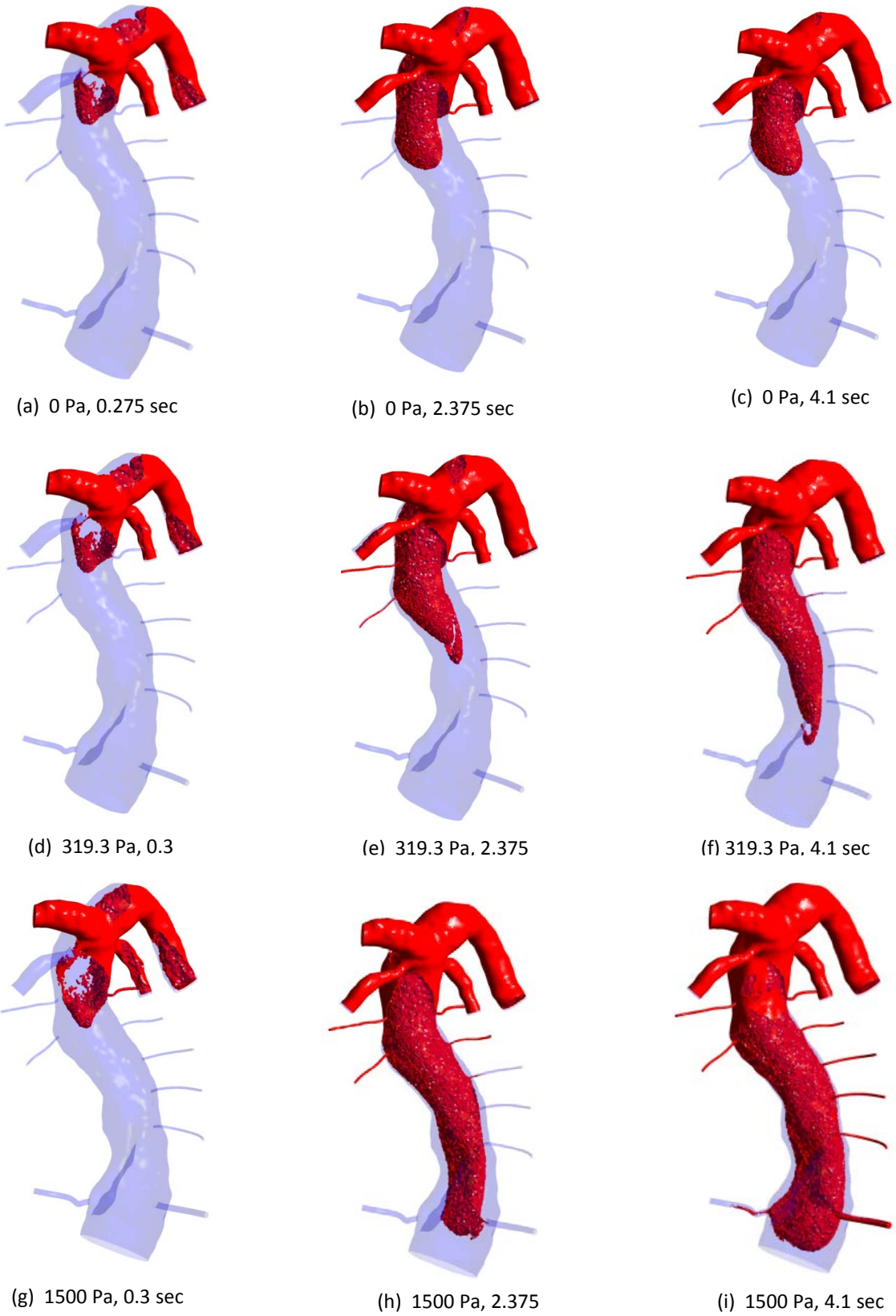

(a) 0 Pa, 0.275 sec

(b) 0 Pa, 2.375 sec

(c) 0 Pa, 4.1 sec

(d) 319.3 Pa, 0.3

(e) 319.3 Pa, 2.375

(f) 319.3 Pa, 4.1 sec

(g) 1500 Pa, 0.3 sec

(h) 1500 Pa, 2.375

(i) 1500 Pa, 4.1 sec

Figure 4-22: Tracer Study: Pressure and Time Comparison

5. Conclusions and Future Work

The simulations in the previous chapter demonstrate that, exception for the perforator location results, outlet geometry has a strong influence on both outlet flow distribution and flow patterns. Some of the results bring to light certain pitfalls which can be avoided if accounted for during model construction, while others show the need for further analysis to predict the impact of the geometry changes accurately.

5.1. Results Analysis

5.1.1. AICA Length

There were two significant findings with the results from the AICA length studies. First, the resistance caused by wall length can be approximated with a static distal pressure. The relationship between wall length and pressure used to emulate it is nonlinear. Based on the flow patterns in Figure 4-2 and Figure 4-4, the flow patterns will be significantly altered if there is no outlet wall present. The minimum length required to eliminate this disruption was not determined in this thesis.

The second significant finding in the length studies is highlighted by the iterative calculations shown in Table 4-1. The distribution of flow among the various outlets can be easily changed with a change in resistance at an outlet; either from increased wall length or an applied pressure. Care must be taken when creating these features to balance their relative lengths so that the simulation does not incorrectly favor one outlet over another. A reasonable approach may be to model the AICAs and perforators with the shortest wall length possible without disrupting the flow patterns, then to apply a distal pressure at each of them, adjusting the pressure to reach the desired outlet flow distribution.

5.1.2. **Perforator Quantity**

The area increase caused by the greater number of perforators has an almost linear relationship with the overall percentage of outlet flow.

Changing the number of perforators has minimal impact on the flow streamline patterns. There is a small decrease in the flow velocities at the lateral branches as the number is increased, which is expected.

There may be value in performing a more detailed investigation involving the addition or removal of a perforator very near to an aneurysm to look for any changes in flow behavior where the flow is already disrupted. Rather than changing perforator quantity, such a study could also be viewed as an expansion of the perforator location study.

5.1.3. **Lateral Branch Diameter**

The diameters of both the AICAs and perforators were increased by a set value for this study. This change adds two difficulties in analyzing the results. First, the use of the same value for the diametrical increase when the initial diameters are different between the two outlet types results in two different area changes. Second, changing the diameters of two different branch types in the same set of simulations, even though both are being analyzed in this thesis, is changing two distinct parameters simultaneously.

From a pure geometry standpoint, this study involves the same change as that in the perforator quantity study: an increase in lower outlet area. The results show this not to be entirely the case. This difference is primarily due to the way wall friction scales at different rates between the two methods of increasing the outlet areas.

For laminar flow at this scale, the resistance to flow due to wall friction can be approximated using Poiseuille's Law (48):

$$R = \frac{8\eta L}{\pi r^4} \quad \textbf{(5-1)}$$

Resistance to flow "R" is inversely proportional to flow rate. Assuming blood viscosity "η" and wall length "L" to be constant; the only change in the system affecting the equation is the increase in radius. The constants can be grouped into one factor "C" for convenience:

$$Q = Cr^4 \quad \textbf{(5-2)}$$

$$\frac{Q_1}{r_1^4} = \frac{Q_2}{r_2^4}, \qquad or \qquad \frac{\Delta(r^4)}{r^4} = \frac{\Delta Q}{Q} \quad \textbf{(5-3)}$$

Table 4-5 shows a comparison of percent increase in the fourth power of the radius to the percent increase in flow rate. The average r^4 of the AICAs increased by just over 150%, while the flow rate increased by only 126.5%. With the perforators, there was an average increase of 586% in their r^4 value, with a 509% increase in flow.

The results can be calculated as an 84.1% "efficiency" in the AICA size increase and 86.9% for the perforators. This discrepancy is likely due to the same phenomenon present in the perforator quantity study; where the increase in outlet area in the lateral branches also increases the total outlet area for the system.

Another possible contributing factor is the mesh at the outlets being too coarse to represent the flow accurately. This possibility is far more likely with the smaller perforators, as they have the lowest mesh density, but that would imply that the AICAs would have better results, which is not the case. It is still worth considering for further analysis.

Both types of lateral branches in the "large" version of the geometry show a greater WSS throughout (see Figure 4-10 and Figure 4-11), which indicates a higher velocity through the outlet; low WSS is indicative of slow moving or stagnant blood (49). The more likely source of this "loss" would be the increased velocity of the blood flow as it enters the lateral branches. In this case, the losses would be largely attributed to the sharp transition at the junction between the outlet and the basilar wall. It may be informative to perform a study where smoother transition radii are added where these features join the basilar artery and compare with these models to see if the sharp transition is indeed a factor.

5.1.4. **Perforator Location**

Changing the locations of the perforators does not appear to have a significant impact on the flow performance.

The WSS directly adjacent to where a given perforator extrudes from the basilar artery is slightly higher than elsewhere on the basilar wall, and moving a perforator appears just to be moving this region of elevated WSS accordingly. If simulation results are being reviewed for WSS behavior near other features in the basilar artery, the location of the perforators may become important as the localized increase in WSS may skew the results of the study.

5.2. **Apex Pressure Studies**

The results from these simulations reaffirm the findings in the AICA length studies; a constant pressure value can be used to replace outlet length to achieve a similar flow distribution.

Applying the same distal pressure to the apex outlets of the "sump" version of the Patient 2 showed only a small change in flow distribution. Both groups of lateral branches saw an increase in their percentage of total flow; 0.404% increase for perforators, 0.830% increase for the AICAs when compared to the "preop" model. It is likely that fewer apex outlets contributed to the larger volume of blood flow to the lateral branches.

It appears that the same distal pressure can be applicable to both versions of the patient geometry. Further testing would need to be performed to verify this conclusion with other physiologies or surgical procedures. It is important to note that different sets of transient data were used for the two models. Comparing the percentage of total flow rather than flow magnitude was an attempt to compensate for this, but there will be different WSS and general flow dynamics due to the different velocity profiles which may affect the results.

When comparing the results of the two "sump" models, columns two and three in Figure 4-20, the large-scale ratio between apex and lateral flow are similar between the two, which would indicate that the apex pressure value determined for patient 2 is close to what would be suitable for patient 1. When viewing the individual outlet groups, there appears to be a large shift in blood flow from SCA to PCA in the patient 1 sump version, and a shift from the perforators to the AICAs.

Each patient will have different flow paths and blood vessel sizes, and the transient data differs between the two. Even accepting those factors, there was no consideration taken in keeping the AICA and perforator diameters and lengths equivalent between the two base models, and there are far fewer perforators included in the patient 1 model. With all of these differences, a direct comparison of the results is more interesting than informative.

The outlet distribution values determined in the final study using the Patient 1 "bypass" geometry cannot be reasonably compared to the results from the other studies. In addition to the differences in perforators and AICAs, this model has only a single apex outlet, which drastically shifts the outlet distribution towards the lower outlets, even without the increase in distal pressure. A more reasonable comparison is to view the changes in flow patterns between simulations performed with no added apex pressure and one with a 319.3 Pa pressure, as is shown in Figure 4-19. In this comparison, there is no significant change in the flow patterns or velocities, indicating a minor change in behavior if any.

In each of the previous studies, particularly the ones using the "sump" models, the flow streamlines were significantly changed with the application of a distal pressure (Figure 4-18). This tendency would seem to indicate that some value of distal pressure, or other resistive force, should be applied to the apex outlets for the flow in these simulations to behave accurately.

5.3. **Tracer Study**

The apex pressure study appears to have reasonable results, yet the results of the tracer study revealed this pressure to be insufficient.

There are several possible reasons for this difference. One, the method of data analysis for the apex pressure study grouped all of the perforators together as one outlet for ease of data handling. It is possible that the majority of the blood exits the perforators nearest the apex which would explain the difference in the outcomes. However, as shown in Figure 4-20, the percentage of total flow exiting the AICAs does not decrease as would be expected if this were the case.

Another possibility is that a single cardiac cycle is insufficient to show blood flow behavior accurately. This observation is similar to the one made by Vignon-Clementel et al. (15) which showed a minimum of 2 cardiac cycles to achieve a stable solution. This appears to be confirmed in the fill patterns illustrated in Figure 4-21 which seem to indicate an initial surge in fill rate which tapers off as the simulation continues.

It is also a good possibility that the 90%/10% apex/lateral flow ratio assumption was not accurate for this physiology.

It is important to note that a pressure value of 1500 Pa value is far greater than what would be expected in actual human anatomy. This result means that either the “sump” surgical procedure will not have a positive outcome for this patient.

The top row of Figure 4-21 shows the results without any additional distal pressure applied at the apex. Fresh blood does not get beyond a certain region of the basilar artery, simply recirculating in the middle. This stagnant flow highlights the need to have a value of distal pressure at the apex outlets. It also brings into question the results of the geometry studies where no such pressure was applied.

The right AICA was consistently the last outlet to fill. The results of the focused analysis, shown in Figure 4-22, are intended to see if there was complete fill at an earlier time step, which may have receded between cardiac pulses. The tracer agent does surge around step 152, but does not recede between cycles; rather, it either remains stationary or fills very slightly in the next two images. In this simulation, at least, there appears to be no recession of blood.

Taking another look at Figure 4-22, the lower half of the right AICA at the basilar wall does not seem to be allowing the tracer agent to pass through, creating a restriction in the flow. It is possible that there is a discontinuity in the model at this junction which would be a strong contributor to the slow fill rate of the AICA.

5.4. **Summary**

The results of these studies have successfully shown which features have a greater or lesser impact on the flow patterns in the simulations. Some features, such as a minimum length of outlet wall, have been identified as being essential requirements for a successful simulation. Some of the findings show the need for further investigation, as described in the next section, but the overall goals of the project were achieved.

5.5. **Future Work**

Increased understanding of the impact of any of these changes would improve their overall utility to control the performance of the models. There are several findings which would benefit from either a greater breadth of data to fill in the gaps or from a deeper analysis in a particular direction of study.

The AICA length studies showed the need for a minimum outlet length for proper flow patterns. Rather than a length value, this is more likely a minimum aspect ratio, which could be tied to outlet diameter, basilar artery diameter, or a combination.

The diameter studies could benefit from more data points to define a stronger trend. The comparison between the outlet diameter study and perforator quantity study might be more meaningful if the diameters of the perforators were increased rather than the perforators and AICAs both. The perforators branch off from the basilar artery nearly perpendicularly. The angle of these with respect to the basilar artery will change the WSS in these regions (50). It may be informative to perform an investigation into the effect of changing these angles.

In the studies investigating the geometry changes, the pressure value at the apex outlets was set to 0 Pa. The percentage of flow through the lateral branches in those simulations was well below 10% of the total flow. This caused some level of difficulty when comparing the results between versions as there were often very small differences between the models. Repeating any or all of these simulations with distal pressure applied to the apex outlets would increase flow to the branches allowing for a better resolution of differences in the results.

During analysis of flow distribution, the output from ANSYS was configured to group all of the perforators as one single outlet. This method simplified the data analysis but may have contributed to errors in situations such as the sump models where the perforators near the apex are likely to see greater flow than those lower on the basilar artery. Although it may not be necessary to have these separate, it would be informative to perform at least one simulation in such a case to see if there is any validity to this concern.

Any of the assumptions listed in Section 3.2.2 can be addressed in a future study, confirming that a more realistic representation displays similar comparisons between the model versions. One of the fundamental assumptions in several of the studies is constant distal pressure, which was shown in the research by Vignon-Clementel et al. (15) to be less accurate than using an impedance model. It may be worth investigating using an impedance model in future studies building off of this research, particularly if performing Fluid Structure Interaction (FSI) simulation.

BIBLIOGRAPHY

1. Hemodynamics of Cerebral Aneurysms. ***Sforza, D M, Putman, C M and Cebral, J R.*** *January 2, 2009, Annu Re Fluid Mech, Vol. 41, pp. 91-107.*

2. Intracranial Aneurysms. ***Schievink, Wouter I.*** *1997, New England Journal of Medicine, Vol. 336, pp. 28-40.*

3. Contemporary Management of Incidental Intracranial Aneurysms. ***Tummala, Ramachandra P, Başkaya, Mustafa K and Heros, Roberto C.*** *2005, Neurosurg. Focus, Vol. 18.*

4. Endovascular Treatment of Unruptured Aneurysms: Systematic Review and Meta-Analysis of the Literature on Safety and Efficacy. ***Naggara, Oliver N, et al.,*** *3, 2010, Radiology, Vol. 256, pp. 887-897.*

5. Computational Modeling of Flow-Altering Surgeries in Basilar Aneurysms. ***Rayz, V L, et al.,*** *May 2015, Ann Biomed Eng, Vol. 43(5), pp. 1210-22.*

6. Fluid Mechanics of Mixing in the Vertebrobasilar System: Comparison of Simulation and MRI. ***Bockman, M D, et al.,*** *2012, Cardiovascular Engineering and Technology, Vols. 3, No. 4, pp. 450-461.*

7. Efficient Pipeline for Image-Based Patient-Specific Analysis of Cerebral Aneurysm Hemodynamics: Technique and Sensitivity. ***Cebral, J R, et al.,*** *2005, IEEE Trans. Med. Imag., Vol. 24, pp. 457-467.*

8. Tuberothalamic Infarct After Division of a Hypoplastic Posterior Communicating Artery for Clipping of a Basilar Tip Aneurysm: Case Report. ***Regli, L and de Tribolet, N.*** *1991, Neurosurgery, Vol. 28(3), pp. 456-459.*

9. Evaluation of the Pontine Perforators of the Basilar Artery Using Digital Subtraction Angiography in High Resolution and 3D Rotational Technique. ***Lescher, S., Samaan, T. and Berkefeld, J.*** *Oct 2014, Am J Neuroradiol, Vol. 35, pp. 1942-47.*

10. CFD for Evaluation and Treatment Planning of Aneurysms: Review of Proposed Clinical Uses and Their Challenges. ***Chung, B and Cebral, J R.*** *January 2015, Annals of Biomed Engrg, Vols. 43, No. 1.*

11. Cerebral Aneurysms Fact Sheet. National Institute of Neurological Disorders and Stroke. *[Online] NINDS, 2013. http://www.ninds.nih.gov/disorders/cerebral_aneurysm/detail_cerebral_aneurysms.htm.*

12. Hemodynamics of Cerebral Aneurysms: Computational Analyses of Aneurysm Progress and Treatment. ***Jeong, Woowon and Rhee, Kyehan.*** *: Hindawi Publishing Corporation, 2012, Computational and Mathematical Methods in Medicine, Vol. 2012.*

13. Giant Intracranial Aneurysms: Evolution of Management in a Contemporary Surgical Series. ***Sughrue, M E, et al.,*** *December 2011, Neurosurgery, Vol. 69(6), pp. 1261-1271.*

14. The International Cooperative Study on the Timing of Aneurysm Surgery. Part 1: Overall Management Results. ***Kassell, N F, et al.,*** *1990, J Neurosurg, Vol. 73, pp. 18-36.*

15. Outflow Boundary Conditions for Three-Dimensional Finite Element Modeling of Blood Flow and Pressure in Arteries. ***Vignon-Clementel, I E, et al.,*** *2006, Comput. Methods Appl. Mech. Engrg., Vol. 195, pp. 3776-3796.*

16. Oscillatory Flow in Arteries: The Constrained Elastic Tube as a Model of Arterial Flow and Pulse Transmission. ***Womersley, J R.*** *2, 1957, Phys. Med. Biol., pp. 178-187.*

17. ***Anliker, M, et al.,*** *Prediction of Shape Changes of Propagating Flow and Pressure Pulses in Human Arteries. [ed.] R D Bauer and R Busse.* The Arterial System: Dynamics, Control Theory and Regulation. *: Springer Berlin Heidelberg, 1978, pp. 15-34.*

18. Structured Tree Outflow Condition for Blood Flow in Larger Systemic Arteries. ***Olufsen, M S.*** *1999, Am J. Physiol, pp. H257-H268.*

19. Blood Flow Dynamics in the Vertebrobasilar System: Correlation of a Transparent Elastic Model and MR Angiography. ***Chong, B W, et al.,*** *April 1994, Am J. Neurorad, Vol. 15, pp. 733-745.*

20. Analysis of Slipstream Flow in a Wide-necked Basilar Artery Aneurysm: Evaluation of Potential Treatment Regimens. ***Imbesi, S G and Kerber, S G.*** *2001, Am J. Neuroradiol, Vol. 22, pp. 721-724.*

21. Imaging of Giant Cerebral Aneurysms. ***Tollard, E., et al.,*** *2014, Neurochirugerie.*

22. Simulation of the Human Intracranial Arterial Tree. ***Grinberg, Leopold, et al.,*** *2009, Philosophical Transactions of the Royal Society A, Vol. 367, pp. 2371-2386.*

23. Image-Based Computational Simulation of Flow Dynamics in a Giant Intracranial Aneurysm. ***Steinman, D A, et al.,*** *2003, Am J of Neurorad, Vol. 24, pp. 559-566.*

24. Computational Fluid Dynamics Modeling of Intracranial Aneurysms: Effects of Parent Artery Segmentation on Intra-Aneurysmal Hemodynamics. ***Castro, M A, Putman, C M and Cebral, J R.*** *September 2006, Am. J. Neurorad., Vol. 27, pp. 1703-09.*

25. Clinical Application of Image-Based CFD for Cerebral Aneurysms. ***Cebral, J R, et al.,*** *7, 2011, Int j numer method biomed eng., Vol. 27, pp. 977-992.*

26. Computational Fluid Dynamics Modeling of Intracranial Aneurysms: Qualitative Comparison with Cerebral Angiography. ***Cebral, Juan R, Putman, Christopher M and Pergolizzi, Jr., Richard S.*** *7, 2007, Academic Radiology, Vol. 14.*

27. Association of Hemodynamic Characteristics and Cerebral Aneurysm Rupture. ***Cebral, J R, et al.,*** *32, 2011, American Journal of Neuroradiology, pp. 264-270.*

28. Prototyping of Cerebral Vasculature Physical Models. ***Khan, Imad S, Kelly, Patrick D and Singer, Robert J.*** *2014, Surgical Neurology International, pp. 5-11.*

29. CFD and PIV Analysis of Hemodynamics in a Growing Intracranial Aneurysm. ***Raschi, M, et al.,*** *2012, Int. J. Numer. Meth. Biomed. Engng., Vol. 28, pp. 214-228.*

30. Complex Flow Patterns in a Real-Size Intracranial Aneurysm Phantom: Phase Contrast MRI Compared with Particle Image Velocimetry and Computational Fluid Dynamics. ***van Ooij, P, et al.,*** *2012, NMR Biomed., Vol. 25, pp. 14-26.*

31. Phase-Contrast Magnetic Resonance Imaging Measurements in Intracranial Aneurysms in Vivo of Flow Patterns, Velocity Fields, and Wall Shear Stress: Comparison with Computational Fluid Dynamics. ***Boussel, L, et al.,*** *2009, Magnetic Resonance in Medicine, Vol. 61, pp. 409-417.*

32. Morphological Studies of the Basilar Artery in Adult Human Cadavers. ***Wankhede, H A.*** *2014, Int J Anat Res, Vol. 2(3), pp. 497-502.*

33. Variations in the Branches of Basilar Artery in Adult Human Cadavers. ***Wankhede, H A, Hosmani, P B and Nimje, D A.*** *2015, Asian Pac. J. Health Sci., Vol. 2(1), pp. 161-166.*

34. Common Features of the Cerebral Perforating Arteries and Their Clinical Significance. ***Djulejć, Vuk, et al.,*** *: Springer-Verlag Wien, 2015, Acta Neurochir, Vol. 157, pp. 743-754.*

35. Normal Anatomical Features and Variations of the Vertebrobasilar Circulation and Its Branches: An Analysis with 64-Detector Row CT and 3T MR Angiographies. ***Akgun, Veysel, et al.,*** *: Hindawi Publishing Corporation, 2013, The Scientific World Journal, Vol. 2013.*

36. Blood Flow Distribution in Cerebral Arteries. ***Zarrinkoob, L, et al.,*** *35, 2015, Journal of Cerebral Blood Flow & Metabolism, pp. 648-654.*

37. ***Steinman, David A.*** Modeling of Physiological Flows. *[ed.] D Ambrosi, A Quarteroni and G Rozza. : Springer-Verlag Italia, 2012.*

38. Influence of Non-Newtonian Flow Behavior on Local Hemodynamics. ***Perktold, K, et al.,*** *1999, ZAMM - Journal of Applied Mathematics and Mechanics, Vols. 79, Supplement S1, pp. 187-190.*

39. ***Bronzino, Joseph D.*** The Biomedical Engineering Handbook. *[ed.] 2nd. : CRC Press, 2000. Vol. I.*

40. Recent Developments in Patient-Specific Image-Based Modeling of Hemodynamics. ***Cebral, Juan R, et al.,*** *Bariloche, Argentina :, 2004, Mecánica Computacional, Vol. XXIII.*

41. ***Blazek, J.*** Computational Fluid Dynamics: Principles and Applications. *Oxford, UK : Elsevier Science Publication, 2005.*

42. ***Khare, Abhishek, Singh, Ashish and Nokam, Kishor.*** Best Practices in Grid Generation for CFD Applications Using HyperMesh. *: Computational Research Laboratories, 2009.*

43. ***Chung, T J.*** Computational Fluid Dynamics. *: Cambridge Univerity Press, 2002.*

44. ***Hoffmann, K A and Chiang, S T.*** Computational Fluid Dynamics. *4th Ed. Wichita : Engineering Education System, 2000. Vol. 1.*

45. ANSYS Fluent Theory Guide. ***ANSYS, Inc.*** *: ANSYS, Inc., 2013, Vol. Release 15.0.*

46. ANSYS Fluent User's Guide. ***ANSYS, Inc.*** *: ANSYS, Inc., 2013.*

47. Toward the Ultimate Concervative Difference Scheme. IV. A Second Order Sequel to Godunov's Method. ***Van Leer, B.*** *: Journal of Computational Physics, 1979, Vol. 32, pp. 101-136.*

48. Dynamics of Pulsatile Flows Through Elastic Microtubes. ***San, Omer and Staples, Anne E.*** *1, March 2012, International Journal of Applied Mechanics, Vol. 4.*

49. Vascular Wall Shear Stress: Basic Principles and Methods. ***Papaioannou, Theodoros G and Stefanadis, Christodoulos.*** *2005, Hellenic J Cardiol, Vol. 46, pp. 9-15.*

50. Combined Effects of Pulsatile Flow and Dynamic Curvature on Wall Shear Stress in a Coronary Artery Bifurcation Model. ***Pivkin, I V, et al.,*** *2005, Journal of Biomechanics, Vol. 38, pp. 1283-1290.*